ESA AO/1-9172/17/I-BG-BALTIC+

BALTIC+ Theme 3
Baltic+ SEAL (Sea Level)

Impact Assessment Report

From: Technische Universität München
Date: 21.12.2020
To: EUROPEAN SPACE AGENCY (ESA-ESRIN)
Subject: **ESA Contract: 4000126590/19/I/BG - BALTIC+ SEAL (Sea Level)**
Category: ESA Express Procurement Plus –EXPRO+
Deliverable: D4.2
Code: TUM_BSEAL_IAR
Authors: Adili Abulaitijiang, Ole Baltazar Andersen, Ida Margrethe Ringgaard, Jacob L., Julius Oelsmann, Felix Müller, Marcello Passaro, Laura Rautiainen, Jani Särkkä
Version: v1.1
Reviewed by: Marcello Passaro
DOI: 10.5270/esa.BalticSEAL.IARV1.1

Accepted by ESA	Signature	Date
J. Benveniste (ESA-ESRIN)		04/02/2021

LIST OF ACRONYMS

ASL: Absolute Sea Level
ATBD: Algorithm Theoretical Basis Document
BS: Baltic Sea
DAC: Dynamic Atmosphere Correction
EOF: Empirical Orthogonal Function
GIA: Glacial Isostatic Adjustment
HR: High-temporal Resolution
IAR: Impact Assessment Report
MDT: Mean Dynamic Topography
MMSL: Multi Mission Sea Level
MSS: Mean Sea Surface
PCA: Principle Component Analysis
RMSE: Root Mean Square Error
RSL: Relative Sea Level
SLA: Sea Level Anomaly
SSH: Sea Surface Height
TG: Tide Gauge
VLM: Vertical Land Motion

Contents

1. Introduction

This document holds the Impact Assessment Report (IAR) prepared by Baltic+ SEAL team, as part of the activities included in the WP4 of the Proposal. The documents present a summary of Experimental Dataset Generation and Impact Assessment. In particular, Section 2 presents the mean sea surface (MSS) model developed by DTU based on the multi-mission sea level products and includes evaluation of the product. Section 3 presents the High-temporal Resolution (HR) grid development and validation with various datasets. Section 4 includes the sea level variability and trend analysis based on the gridded products, as well as Tide Gauges (TG). Moreover, Vertical Land Motion (VLM) trends are estimated by absolute and relative sea level trends from altimetry and tide gauges and evaluated in Section 5.

2. Mean Sea Surface modelling and impact assessment (DTU)

2.1 Mean sea surface modelling

2.1.1 Methodology

The mean sea surface (MSS) of the Baltic Sea is derived in the framework of remove-restore [Forsberg, (1991); Tscherning and Forsberg, (1986); Sjöberg (2005)]. The long wavelength components of the MSS is provided by the DTU15MSS [Andersen et al., (2016)], where a 20-year (1993-2012) period Topex and Jason series set up the bone of the mean sea surface. DTU15MSS has been derived by the data extracted from Radar Altimetry Database System (RADS) [Scharroo et al., (2013)]. In this project, we consider the update of the mean sea surface using both a long and short wavelength correction grid (see section 2.1.5), since there could be residual long wave length errors in the DTU15MSS. In addition, this could also be due to the ALES+ retracker, which is different from Brown retracker [Brown, (1977)], extensively used in RADS.

At the very first step, DTU15MSS is removed from the sea surface heights (SSH) and sea level anomalies (SLA) are obtained for each track.

$$SLA = SSH - DTU15MSS \tag{1}$$

For the Exact Repeat Missions (ERM), all the altimetry data has to be stacked to derive a mean profile. In section 2.1.2, the methods to derive the mean profiles will be described. After deriving the mean profiles, all available data will be crossover adjusted in 1 degree (latitude) by 3 degree (longitude) patches to further minimize the discrepancies at the cross-over points and retrieve the short-wavelength features. The final residual SLAs will be used to derive the short wavelength grid and added to the long wavelength correction grid and DTU15MSS to derive the final mean sea surface of the Baltic Sea.

2.1.2 Deriving mean profiles

The ALES+ retracked dataset covers nearly all ERM mission starting from May 1995 to May 2019. The ERM missions can be grouped as in Table 1 depending on the ground track distribution.

Table 1. List of altimetry missions to be grouped in order to derive the mean profiles. Counts of unique passes and total number of cycles (repeats) on each pass are also presented.

Altimetry missions	Total number of unique passes	Total number of cycles (repeats)
Topex, Jason-1, Jason-2 and Jason3	32	948
ERS-2 and ENVISAT	61	159
Jason-1 and Jason-2 extended mission	31	127
SARAL/AltiKa	61	35

CryoSat-2	497	114
Sentinel-3A and Sentinel 3B	46	42
Sentinel-3B (interleaved)	47	7

The time span of the Topex and Jason series covers entire dataset, i.e., 24 years. The time span of the ERS-2 and ENVISAT ERM extends up to 16 years starting from May 1995 until October 2010. These two groups of missions have the longest temporal coverage and similar to the base frame work of the DTU15MSS. Hence, the long wavelength correction grid is derived based on the stacked mean profiles from the two groups.

In general, the stacked mean profiles will be derived in the following steps:

1. Select a unique pass and read in all cycles with the same pass number from all available missions
2. Fit a second order polynomial regression curve to the geographic locations (latitude & longitude pairs) from all cycles to obtain a virtual reference profile. Since the least square fit is optimal to derive a mean track that approximately pass through the point clusters, a specific cycle close to the reference profile can be considered as the location of the mean profile track. See Figure 1.
3. Cross-track distance between each track (cycle) and the reference profile is calculated and any track further away than 1.5 km is not used for stacking.
4. All tracks within 1.5 km cross-track distance to the reference profile are projected to the reference profile and the sequence of tracks will build up the stack that will be used for deriving the final mean profiles. See Figure 2 and 3.
5. In addition to the least square fitting, each along track SLA in the stack will be detrended first before deriving a numeric mean at each satellite observation point. This is conducted because least square fitting results are noisy when the time series are short (e.g., SARAL/AltiKa, Sentinel-3 series)

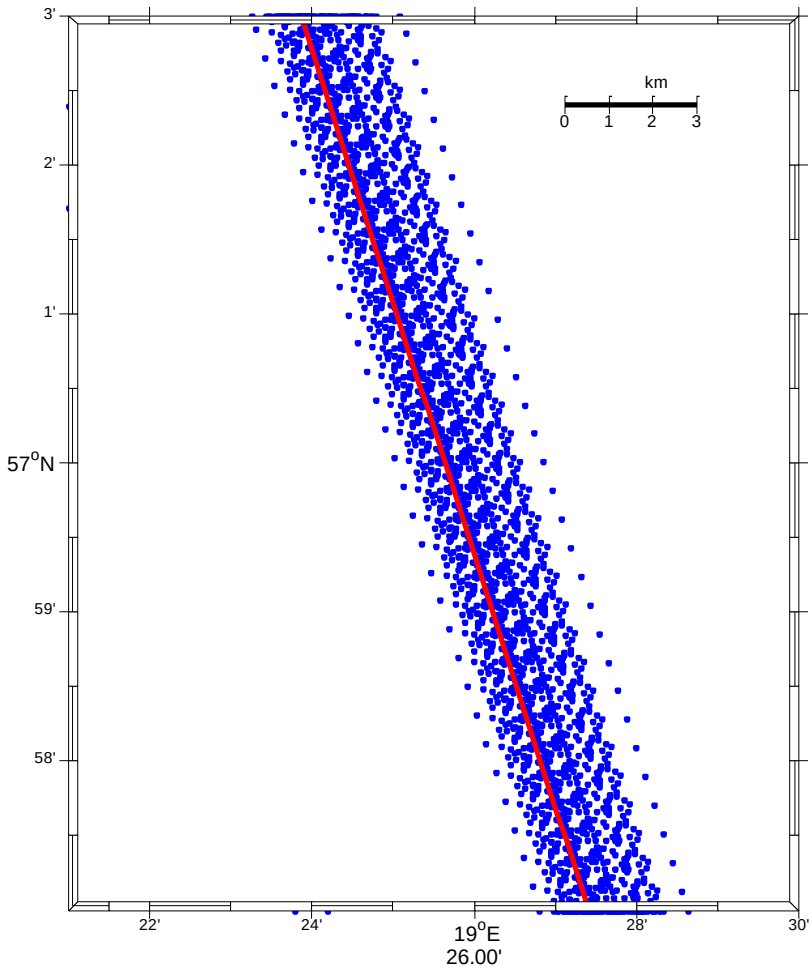

Figure 1. An example of ERS-2 and ENVISAT pass No. 313. There are 159 cycles denoted by the blue dots on this specific pass (track). The red curve passing through the point clusters is derived by least square fitting.

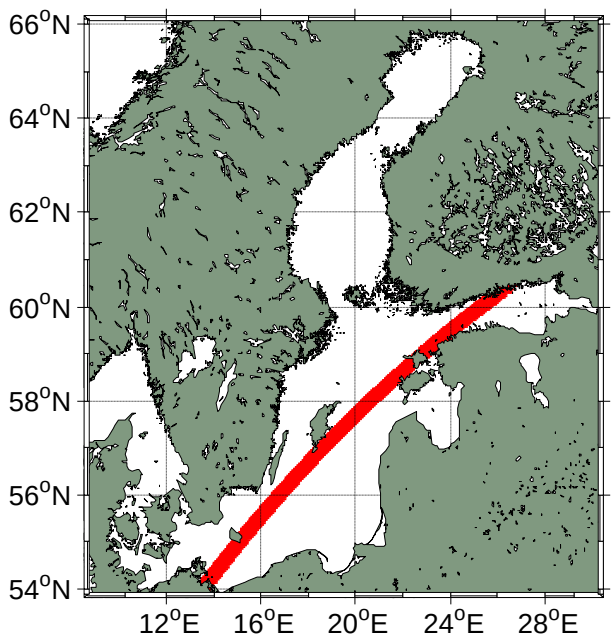

Figure 2. Topex and Jason series pass 111. Satellite is flying from south to north direction, i.e., ascending

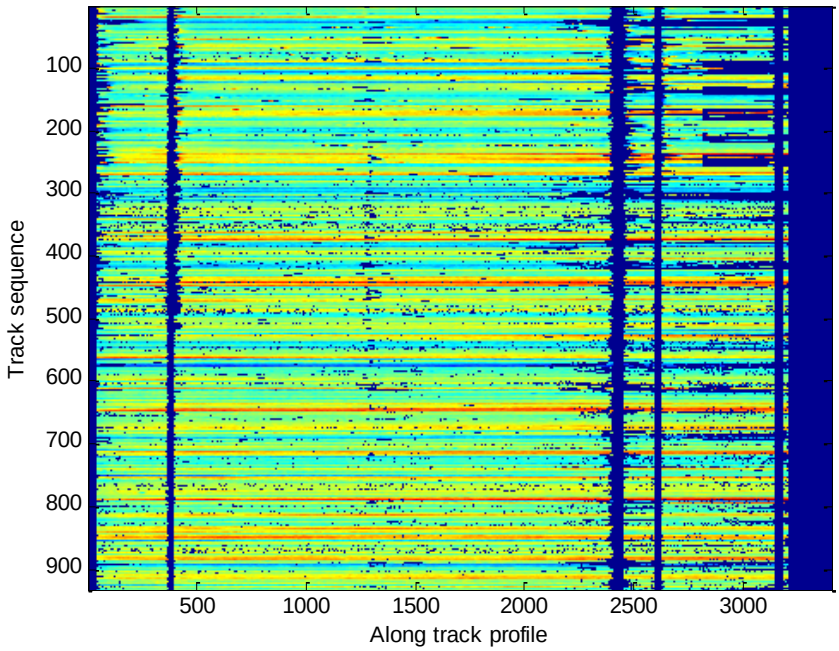

Figure 3. Stack of the along track sea level anomalies along the Topex and Jason series pass 111. In total 932 cycles are available for stacking. The first 268 cycles are for Topex. X-axis denotes along track point sequence along the ascending pass 111.

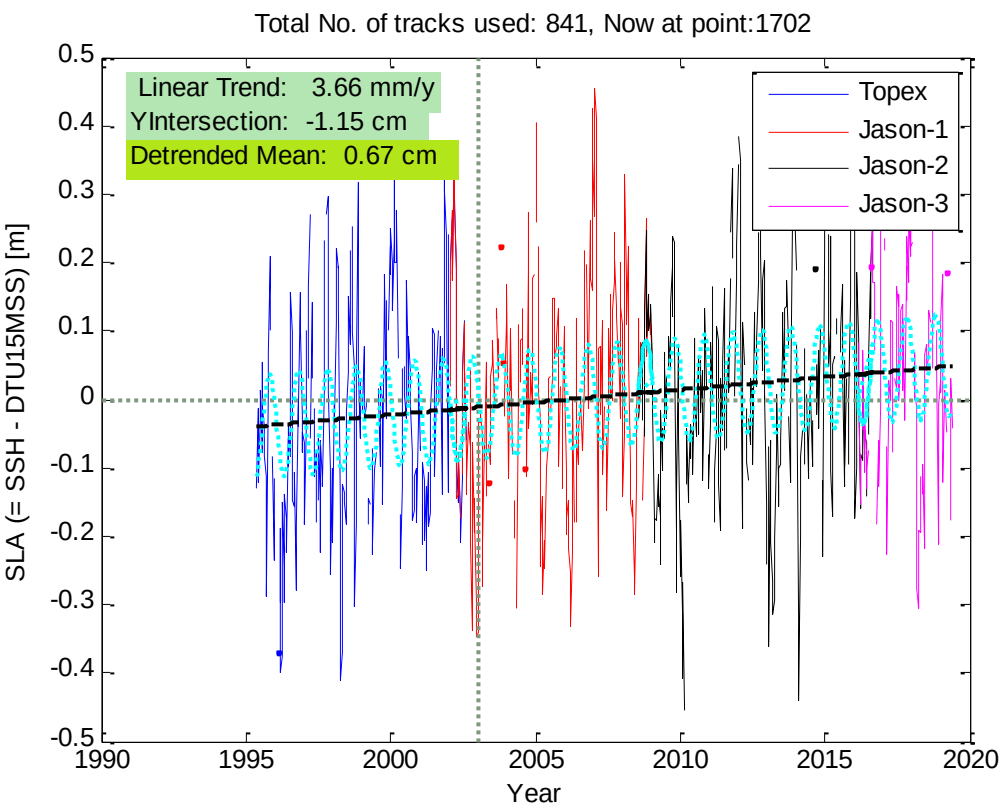

Figure 4. Time series of a single point (location) along the pass 111. This plot illustrates the SLA variation along the column (1702) of stack shown in Figure 3. A linear regression curve (thick dashed black) and harmonic function including linear trend term (dashed cyan color) is superimposed to the time series.

2.1.3 Cross-over adjustment and gridding

After deriving the mean profiles, the along-track mean profiles are edited and checked for potential outliers. In this project, we set a threshold of 5 time standard deviation of the mean SLA to filter out potential outliers from the mean profiles. Figure 5 shows the location where the outliers are located for CryoSat-2 mean profiles. The outlier distribution is similar to other satellites. After obtaining "clean" along track mean profiles, cross-over adjustment [Knudsen and Brovelli, (1993)] is performed in small patches (1×3 degree). These represent short wavelength features, which can be modelled from the ALES+ retracked dataset. In the next step, the data after cross-over adjustment is gridded.

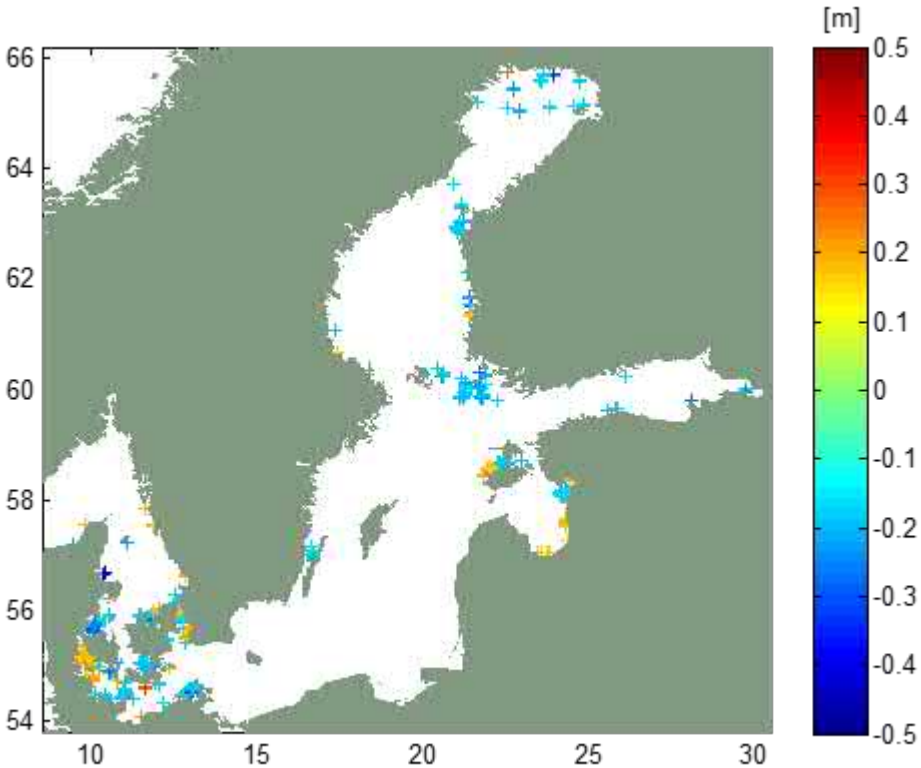

Figure 5. Locations of outliers in the stacked CryoSat-2 mean profiles. The outliers are located mostly near the coast and northern boundary of Gulf of Bothnia, which is covered by seasonal sea ice. Only 0.36% altimetry data among the CryoSat-2 mean profiles is flagged as outliers.

2.1.4 Long wavelength correction grid

The ALES+ retracked altimetry data is cross calibrated and absolute sea surface height is referenced to Topex cycle means. The mean reference period of DTU15MSS is year 2003.0. In an ideal scenario, when the DTU15MSS is removed from SSH, the SLA at the epoch 2003.0 should be zero. However, this is not guaranteed due to either retracker bias or residual cross calibration errors. Moreover, it could also be related to the regional biases residing in DTU15MSS for the Baltic Sea. Hence, we construct a long wavelength correction grid based on the Topex and Jason series, as well as the ERS-2 and ENVISAT time series.

As shown in Figure 4, a harmonic function including a linear trend terms is fitted to the time series at each along track position. The time series has zero epoch at year 2003.0 (dotted gray line). The y-axis intersection of the fitted curve is saved as the correction value with respect to DTU15MSS. After computing all corrections along the Topex/Jason and ERS-2/ENVISAT passes, the data is gridded with 100 km filtering radius to construct long wavelength correction grid.

To reduce the impact of large variation along the coast, altimetry data which has ALES+ quality flag equals to 0 is used when deriving the mean profiles that are to be used for long wavelength correction grid.

Figure 6 shows the long wavelength correction grid and corresponding gridding error map. The gridding error map is simply an indicator of presence of data available for gridding and thus, it should not be considered to be the error of long wavelength correction grid. Since the quality flag is used, large interpolation errors are present near the coast and one can infer, that altimetry data is missing near the Åland Islands close to Finland.

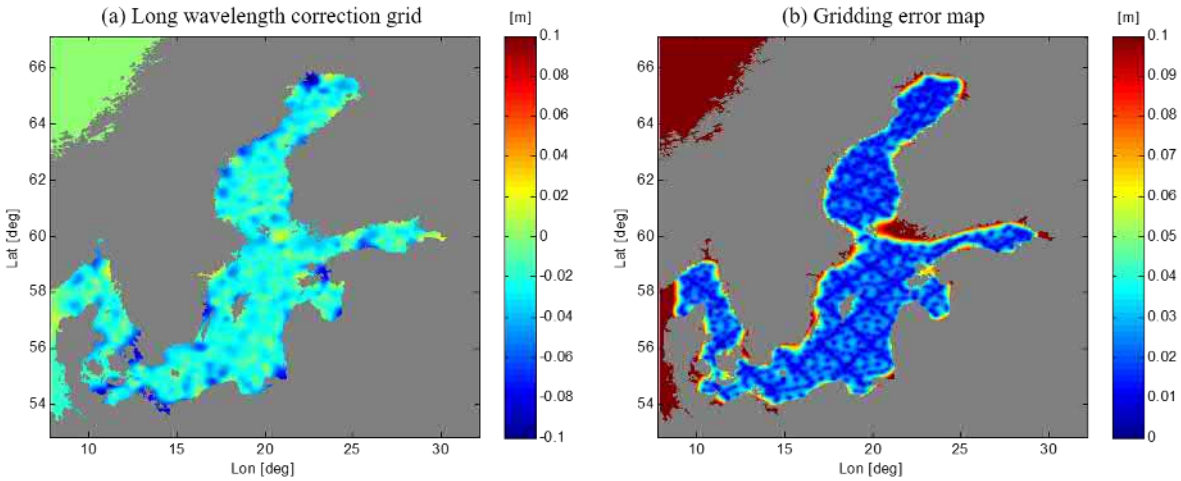

Figure 6. (a) Long wavelength correction grid derived from Topex/Jason series and ERS-2/ENVISAT mean profiles. (b) Corresponding gridding error map.

2.1.5 Final mean sea surface of the Baltic Sea

After deriving the long wavelength correction grid and short wavelength correction grid after the cross-over adjustment procedure in section 2.1.3, the DTU15MSS and afore mentioned two grids are added to construct the final mean sea surface of the Baltic Sea. Note, that the new mean sea surface shown in Figure 7 still corresponds to a mean period of year 2003.0, which is identical to DTU15MSS.

2.2 Mean sea surface model and deliverables

2.2.1 Mean sea surface model of Baltic Sea

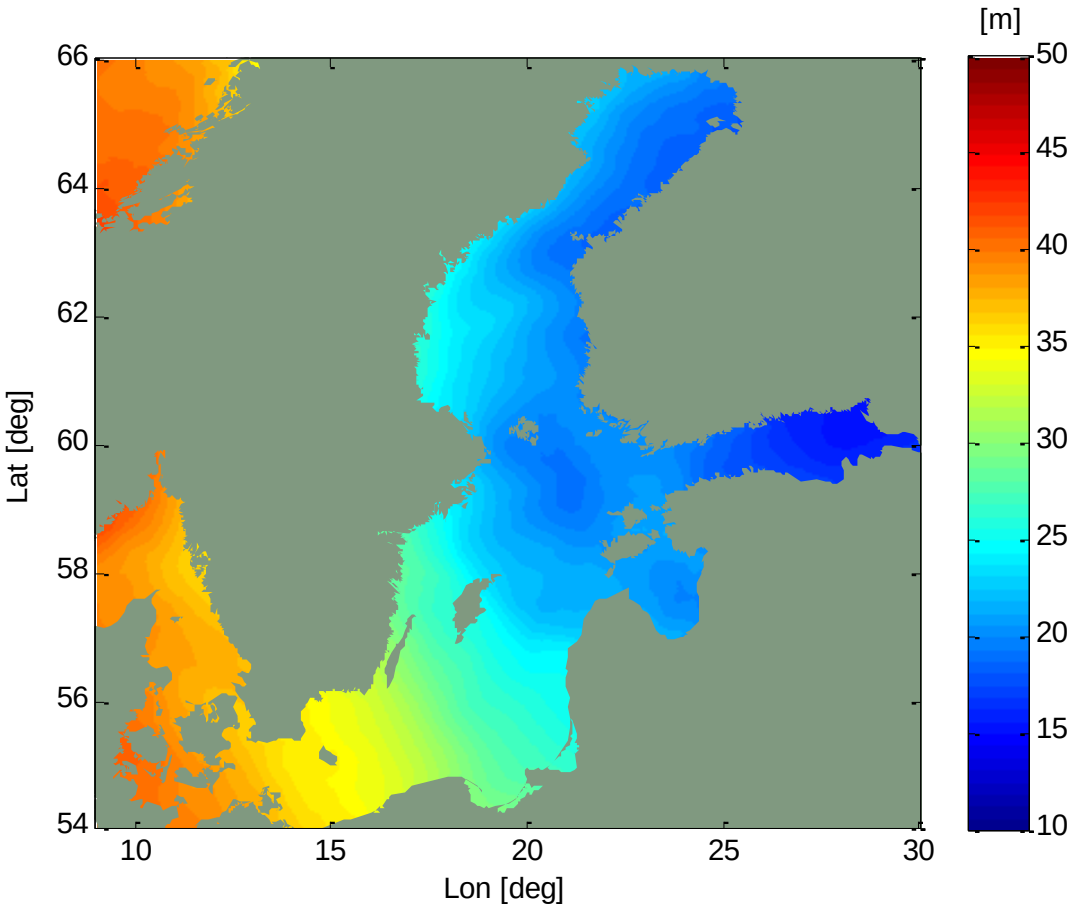

Figure 7. The BalticSEAL Mean sea surface model of the Baltic Sea derived from altimetry data provided by TUM

2.2.2 Gridding error map

The gridding error map of the final mean sea surface is obtained by the theory of error propagation, since it is the sum of long and short wavelength grids.

$$\sigma = SQRT(\sigma_{long}^2 + \sigma_{short}^2) \tag{2}$$

Figure 8 shows the final gridding error map. Note that the σ_{long} from the long wavelength correction grid is the main source in the final gridding error map.

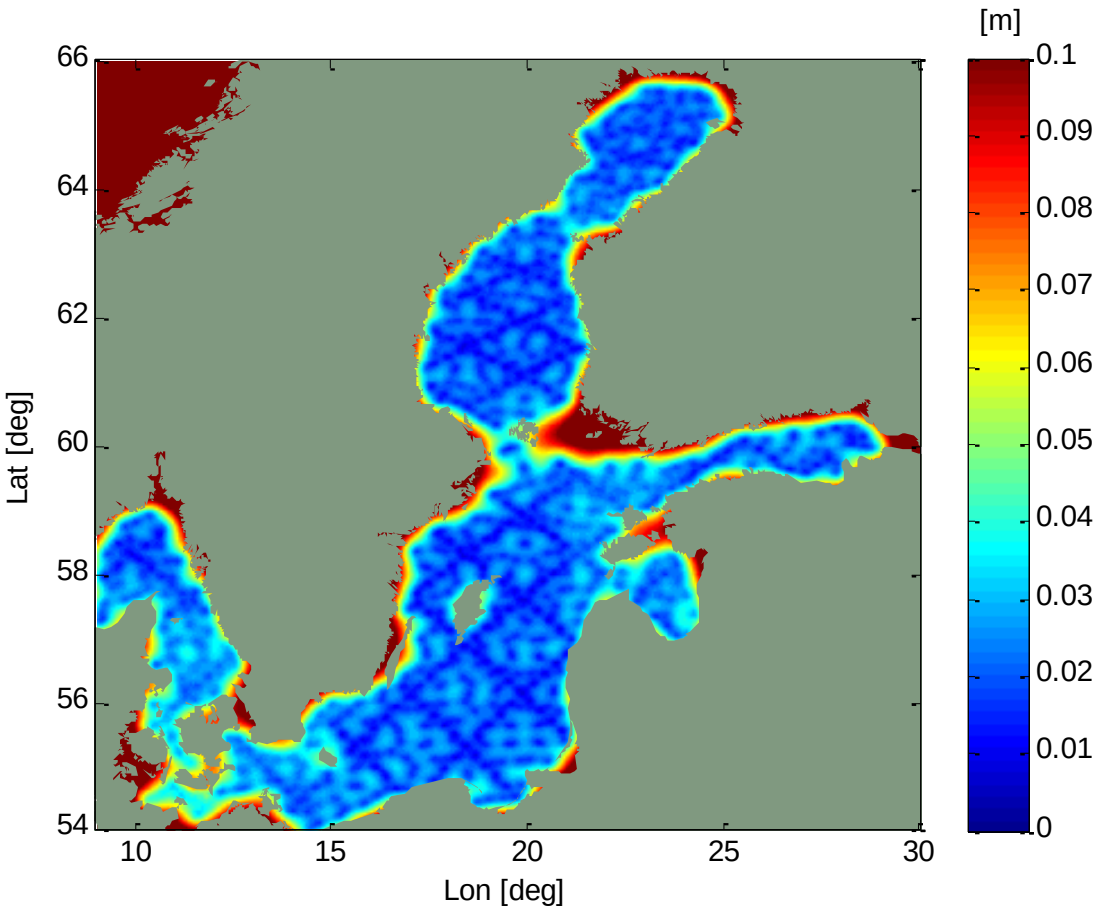

Figure 8. Gridding error map of the final mean sea surface model for the Baltic Sea

2.2.3 Quality mask based on gridding error

For future users of the mean sea surface model, a simple quality mask is generated by a simple threshold of 4 cm on the final gridding error map above. The quality mask (Figure 9) is distributed along with the mean sea surface model.

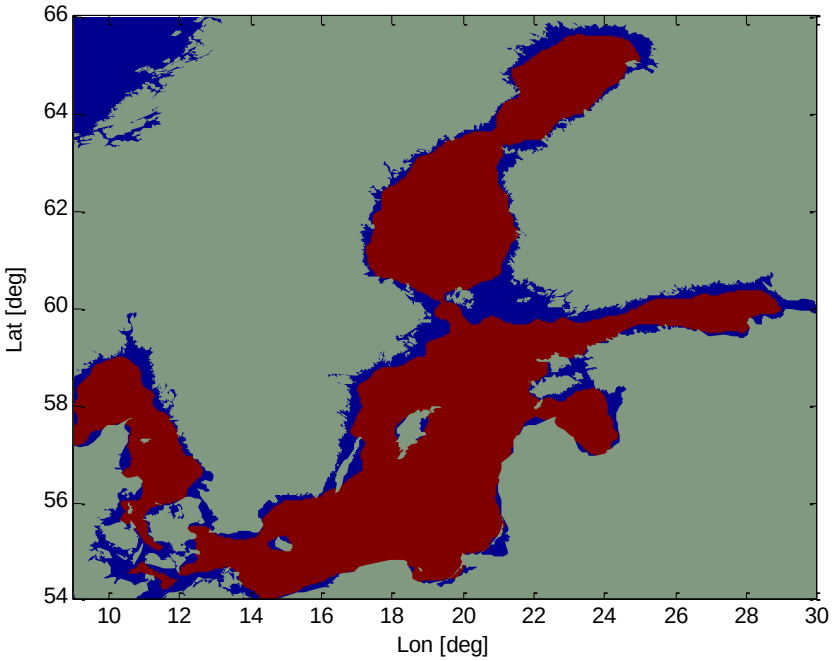

Figure 9. Quality mask based on the gridding error map of the mean sea surface model. Red pixels (flag=0) imply areas with good altimetry data coverage, while blue pixels (flag=1) imply areas with less or no qualified altimetry data coverage.

2.3 Impact assessment

2.3.1 Difference between BalticSEAL MSS and DTU15MSS

The difference between mean sea surface model developed in this project and DTU15MSS is shown in Figure 10. Due to the newly introduced long wavelength correction grid, the new MSS model is approximately 2 cm lower than DTU15MSS. Moreover, considerably large differences can be observed near the coastal zone, Danish Straits and bay of Bothnia. We spotted, that DTU15MSS is unreasonably high near coastline, which is an artifact of gridding due to the lack of data. With high quality data from this project, making the most of qualified observations from ALES+ retracker, costal gaps are partly narrowed down. Hence, one can observe major discrepancies near the coastline in the Baltic region from Figure 10.

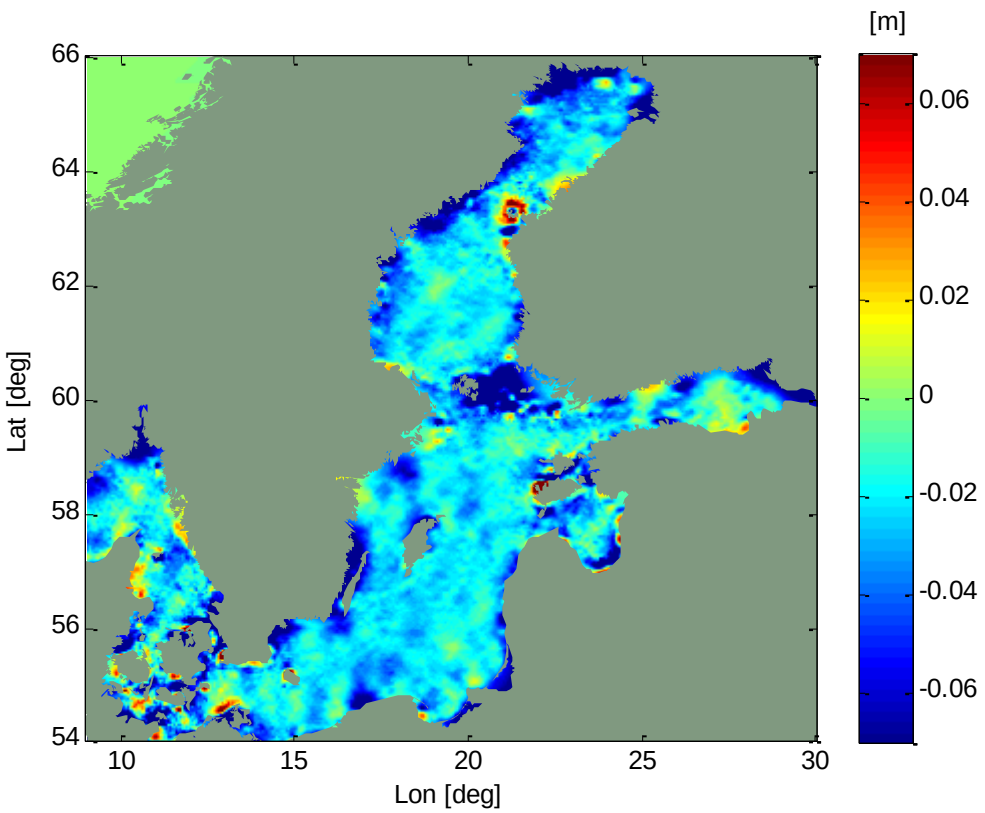

Figure 10. Difference between the new BalticSEAL mean sea surface of the Baltic Sea and DTU15MSS

2.3.2 Assessment using geoid and mean dynamic topography

The quality of mean sea surface model can be evaluated further by deriving mean dynamic topography (MDT). A geodetic mean dynamic topography can be derived by subtracting a geoid model from MSS.

$$MDT = MSS - Geoid \tag{3}$$

Here, we use EGM2008 geoid model to construct the MDT.

MDT derived from the new MSS of the Baltic Sea and DTU15MSS is shown in Figure 11. Due to the large coastal gap in the altimetry data used for DTU15MSS, the MDT derived from DTU15MSS is dramatically high near the coastal zone, e.g., Bay of Bothnia and Swedish coast. The MDT derived from new MSS model of the Baltic Sea is more homogeneous both over the open ocean and near the coast. Major improvement can be observed around the Danish Straits (Figure 12) and Estonian islands (Figure 13). These all attributed to the improvement in the new MSS developed in this project.

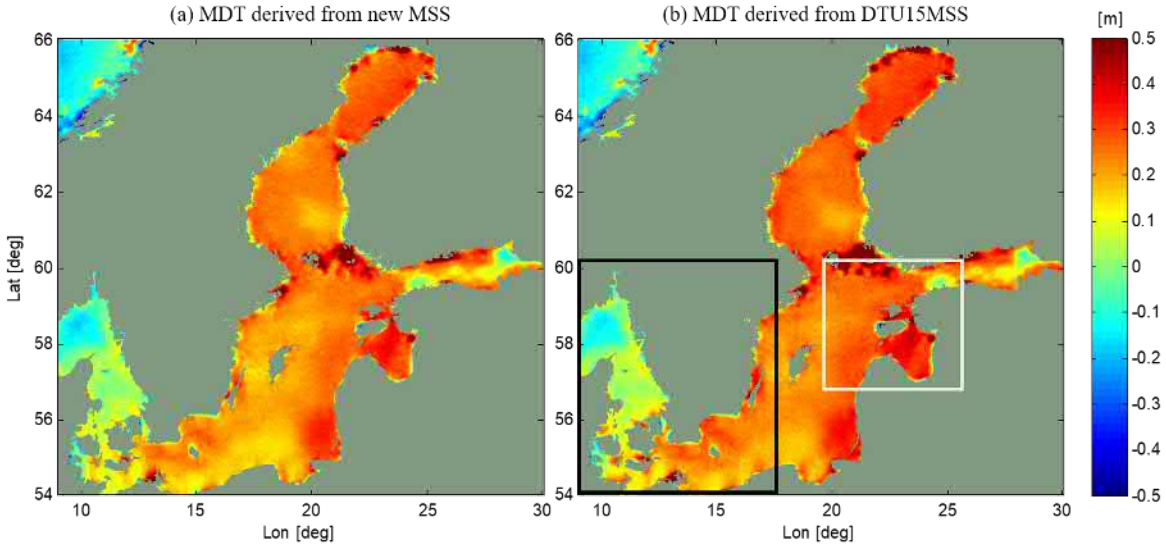

Figure 11. MDT derived from the new MSS of the Baltic region (a) and DTU15MSS (b). MDT around the Danish Straits (black box) and Gulf of Riga and Finland (white box) are shown in Figure 12 and 13.

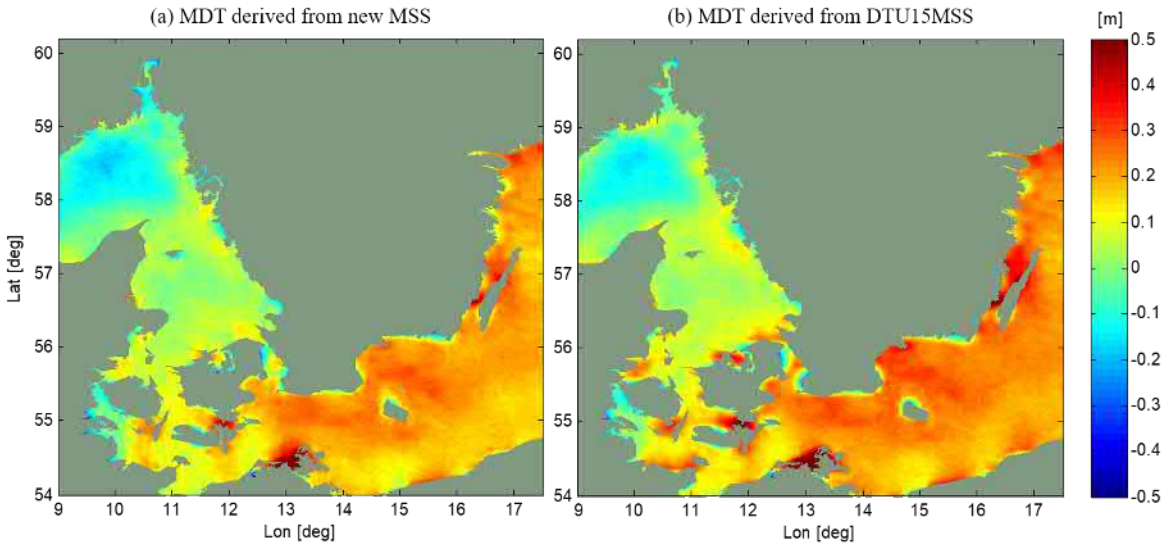

Figure 12. MDT around Danish Straits.

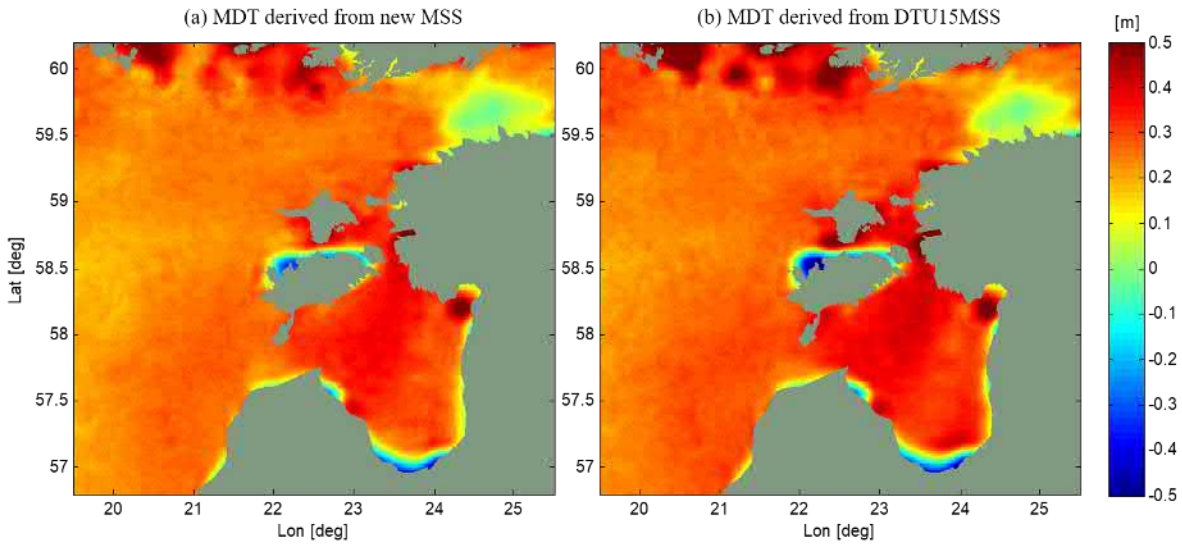

Figure 13. MDT around Gulf of Riga and Finland. Near the Estonian islands the new MSS is slightly improved compared to DTU15MSS

2.3.3 Assessment by mean profiles before and after deriving MSS model

When a new mean sea surface model is developed, the altimetry data used for constructing the new MSS model should fit better to this new MSS model than with other (older) MSS models. Hence, we can derive SLA mean profiles based on the new MSS and then compare them with SLA mean profiles based on DTU15MSS.

Table 2 shows the standard deviation (STD) of SLA mean profiles with respect to the new MSS model and DTU15MSS. Nearly all mean profiles fit better to the new MSS model, although the STDs may suggest the difference are marginally small. As shown in Figure 14, in the Gulf of Riga and Finland, near the Estonian island, the SLA-mean is considerably small and less along track variation can be observed. These imply, that the new MSS model is consistent with the ALES+ altimetry data and improvements are gained in the complex coastal regions.

Table 2. Statistic on SLA mean profiles covering entire Baltic region, Unit: meter

Altimetry missions grouped for stacking	**STD of SLA mean profiles referenced to new MSS**	**STD of SLA mean profiles referenced to DTU15MSS**
Topex, Jason-1, Jason-2 and Jason3	0.013	0.016
ERS-2 and ENVISAT	0.020	0.025
Jason-1 and Jason-2 extended mission	0.019	0.017
SARAL/AltiKa	0.022	0.027
CryoSat-2	0.032	0.038
Sentinel-3A and Sentinel 3B	0.024	0.029
Sentinel-3B (interleaved)	0.028	0.032

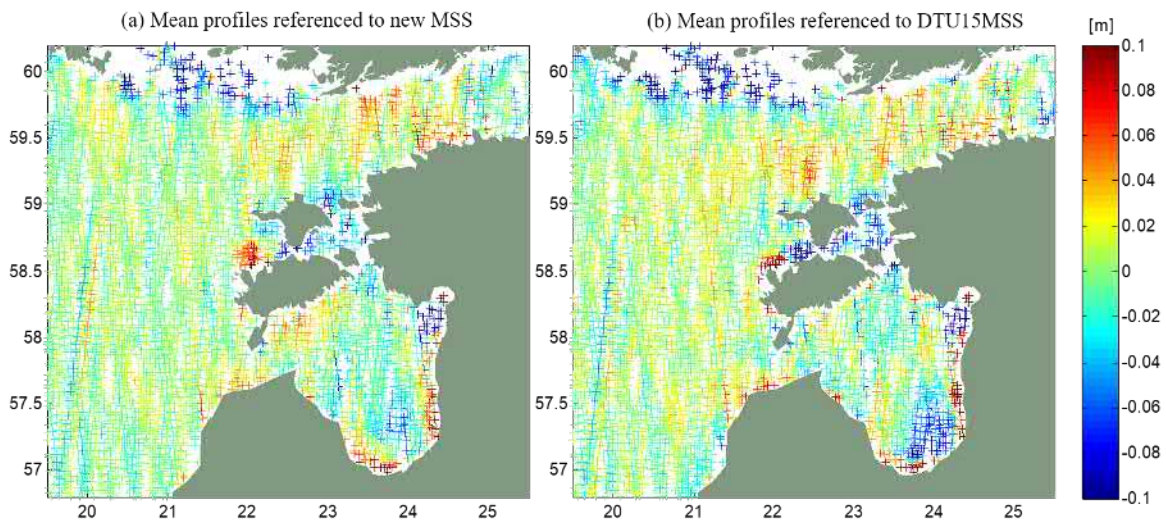

Figure 14. Stacked SLA mean profiles for all ERM missions referenced to (a) the new MSS model of Baltic Sea (b) DTU15MSS

3. Assessment of high-temporal resolution grid (DMI)

3.1 Data set description

The aim of this task is to generate and assess a gridded sea level product of the Baltic Sea on a temporal scale of a few days, combining information from satellite altimetry with tide gauge observations and storm surge model statistics. Due to the infrequent satellite passes over the

Baltic Sea, the main question is whether a sea level product covering a few days at a time can gain sufficient information from satellite altimetry and tide gauge observations to represent the Baltic Sea sea level adequately. This product is evaluated against the monthly mean satellite altimetry product developed by TUM (hereafter referred to as TUM MM).
If successful, this will be an observational product independent from storm surge models and their error sources such as atmospheric forcing, river inflow etc. Potential usages are improving the preconditions leading up to extreme sea level events. To be able to investigate this, the product needs to cover a period with extreme sea level events. We chose year 2017, as there was a surge event in the western Baltic in the beginning of January this year.

3.1.1 Data sources

The three different types of data used to generate the high-resolution gridded product are described in the Dataset Description (Deliverable D2.1). Data is further processed as described below before generating the gridded product.

3.1.1.1 Satellite altimetry

In the year 2017, there are several altimetry missions operating (i.e., Jason-2, Jason-3, CryoSat-2 and Sentinel-3A). By using multi-mission along-track altimetry data, a good spatial and temporal coverage of the Baltic Sea is expected. The altimetry observations from the available missions are extracted with the quality flag and contain the FES2014 ocean tide model. To have sufficient spatial coverage of satellite tracks we decided on using 3-day averages, i.e. January 1st-3rd, 4th-6th etc.

3.1.1.2 Tide gauge observations

For the high-resolution gridded product, tide gauge stations are discarded if the RMSE between tide gauge observations and satellite altimetry where above 0.5m or the correlation was below 0.6.
Similar to the satellite altimetry data tide gauge data is averaged over the same 3-day periods. Raw tide gauge observations refer to the non-averaged observations with original temporal resolution.
The available tide gauge observations are divided into two groups: one for the production of the HR product (Production stations) and one for validation (Validation stations), see Figure 15.

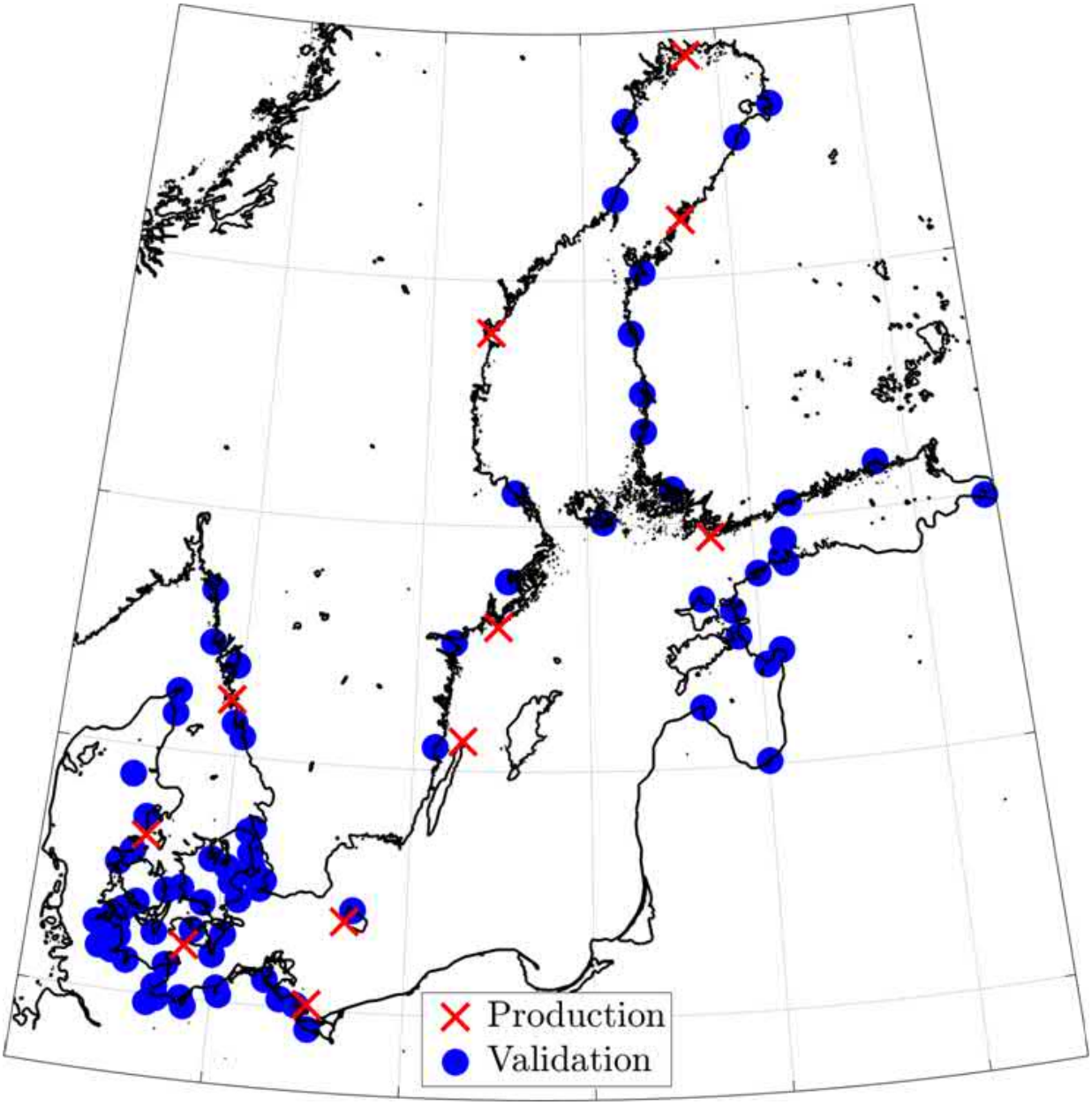

Figure 15. Production (red crosses) and Validation (blue dots) tide gauge stations.

3.1.1.3 Storm surge model

As for the previous two data types, the HBM storm surge model output (http://ocean.dmi.dk/validations/surges/index.uk.php) is averaged over 3 days. Additionally, the standard deviation for the same 3-day periods is computed.

3.1.2 Optimal interpolation method

The DMI Optimal Interpolation (DMI-OI) method used here, is a statistical interpolation system that has been used extensively within Copernicus Marine Environment Monitoring System (CMEMS) to produce gap free SST L4 products (see e.g. Høyer & Karagali, 2016). The DMI-OI system has been modified from its original processing chain and generate here a gridded and gap free estimate of the sea level anomalies (SLA) with respect to the mean sea surface on a spatial grid of 0.02 degrees in latitude and longitude covering the Baltic Sea (east of 90E).

The processing chain of the DMI-OI system is shown in the Figure 16.

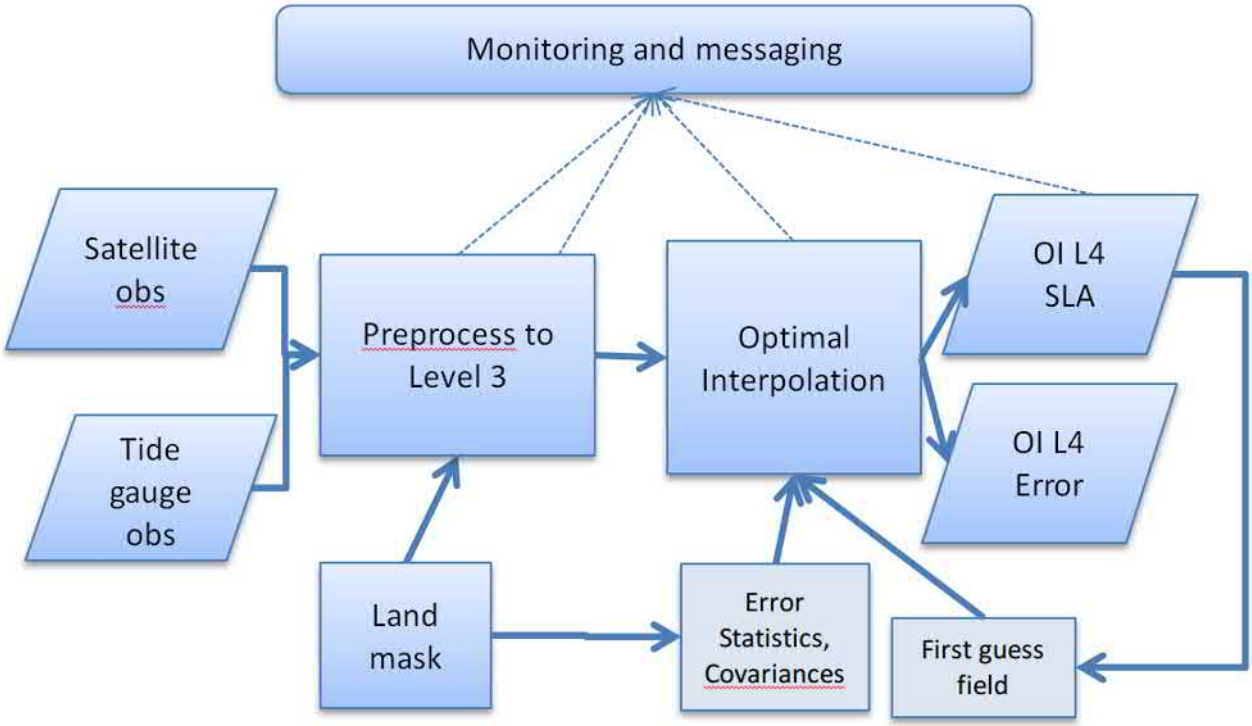

Figure 16. Schematic diagram of the DMI-OI processing chain at DMI

An analysis is performed for every 3 days and satellite and tide gauge for a particular analysis time are processed and aggregated within -+36 hours from the analysis on the Level 3 grid, as described above. The main OI analysis uses a persistence approach, based on the use of a first guess field. The aggregated L3 observations from the current period are calculated as anomalies with respect to the first guess field and local statistics have been used to estimate the optimal estimates SLA values for the final field. The gridding statistics used for this product is a 500 km error covariance length scale, 5 cm uncertainties on the observations and a first guess error variance calculated from the model variability fields. The first guess standard deviation is shown in the Figure 17.

Figure 17. Standard deviation of SLA for the 3-day averaging periods, derived from hourly model simulations and used for the first guess standard deviation in the OI.

Due to the large spatial and temporal variability between each of the 3 days averaging periods, an iterative loop was introduced, where the OI interpolation and anomaly calculation was carried out 5 times, using the OI field from the previous iteration as first guess field. This was to satisfy the OI assumptions that the anomalies to be gridded are bias free and Gaussian distributed. Two types of initial first guess fields have been tested, one where the previous 3 day analysis has been used as first guess and one, where the 3-day averaged model fields have been used. The L4 runs are hereafter referred to as the HR gridded products or, when distinguishing between the two versions, as FGSat and FGModel.

3.2 Validation of the HR gridded product

The HR gridded products are validated by comparing it to the validation tide gauge stations. Figure 18 and Figure 19 show examples from two tide gauge stations. Figure 20 shows the statistical summary for all Validation stations over the full year 2017.

The two HR gridded products are mostly similar to the observed 3-day mean (black crosses) and each other (Figure 18 and Figure 19). However, large and rapid shifts in sea level occur in both

FGModel and FGSat for stations in the eastern and northern part of the Baltic Sea as illustrated in Figure 19.

The statistical overview of the entire year 2017 shown in Figure 20 reveal two main things: 1) The bias of the TUM MM is generally much larger than the bias of the HR gridded products, which is expected since TUM MM is a monthly mean and is being compared with products characterised by a higher temporal resolution 2) FGModel and FGSat are very similar taken over one full year and they have a lower RMSE than TUM MM for most stations. Those stations where TUM MM has a lower RMSE are mainly located in the Gulf of Finland, in the Gulf of Riga or in the Inner Danish Waters.

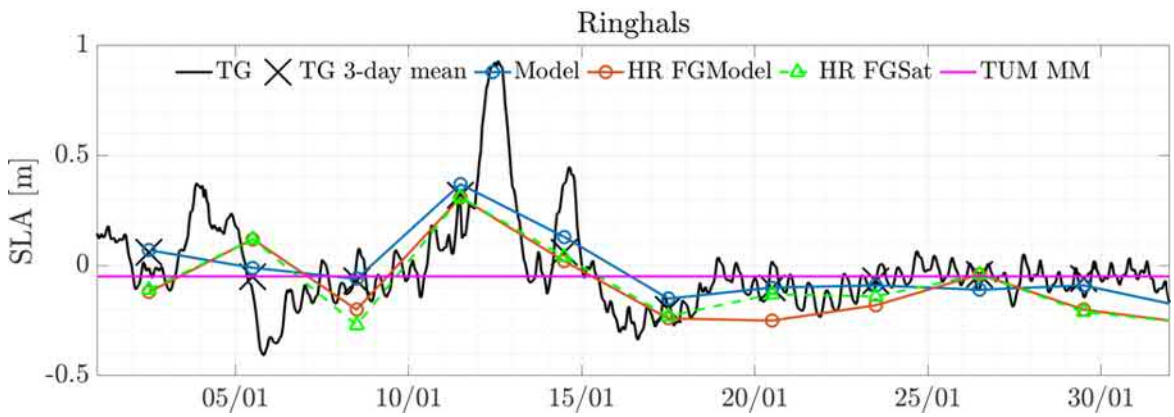

Figure 18. Sea level anomaly (SLA; in m) at Ringhals for the raw tide gauge observation (black line), the 3-day mean of the tide gauge observation (black cross), the modelled sea level (blue circles), FGModel (red), FGSat (green) and the monthly mean altimetry product (TUM MM; pink).

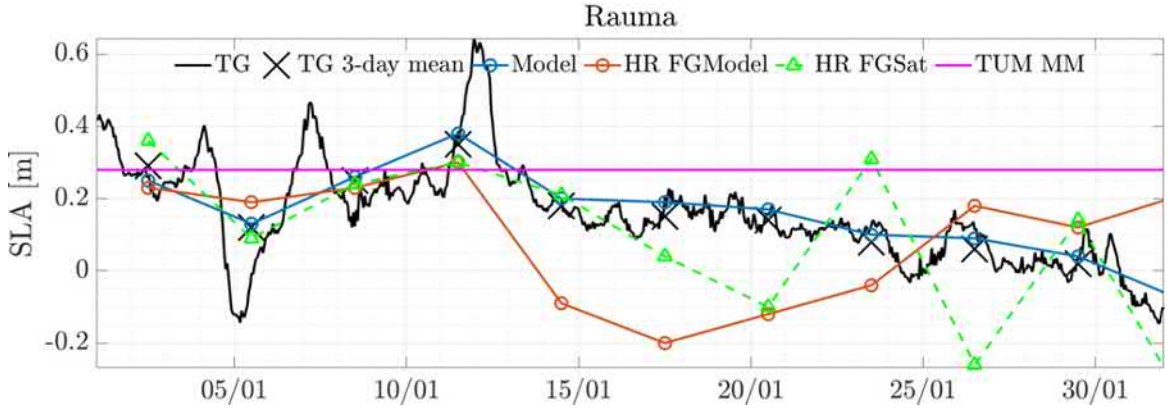

Figure 19. Sea level anomaly (SLA; in m) at Rauma for the raw tide gauge observation (black line), the 3-day mean of the tide gauge observation (black cross), the modelled sea level (blue circles), FGModel (red), FGSat (green) and the monthly mean altimetry product (TUM MM; pink).

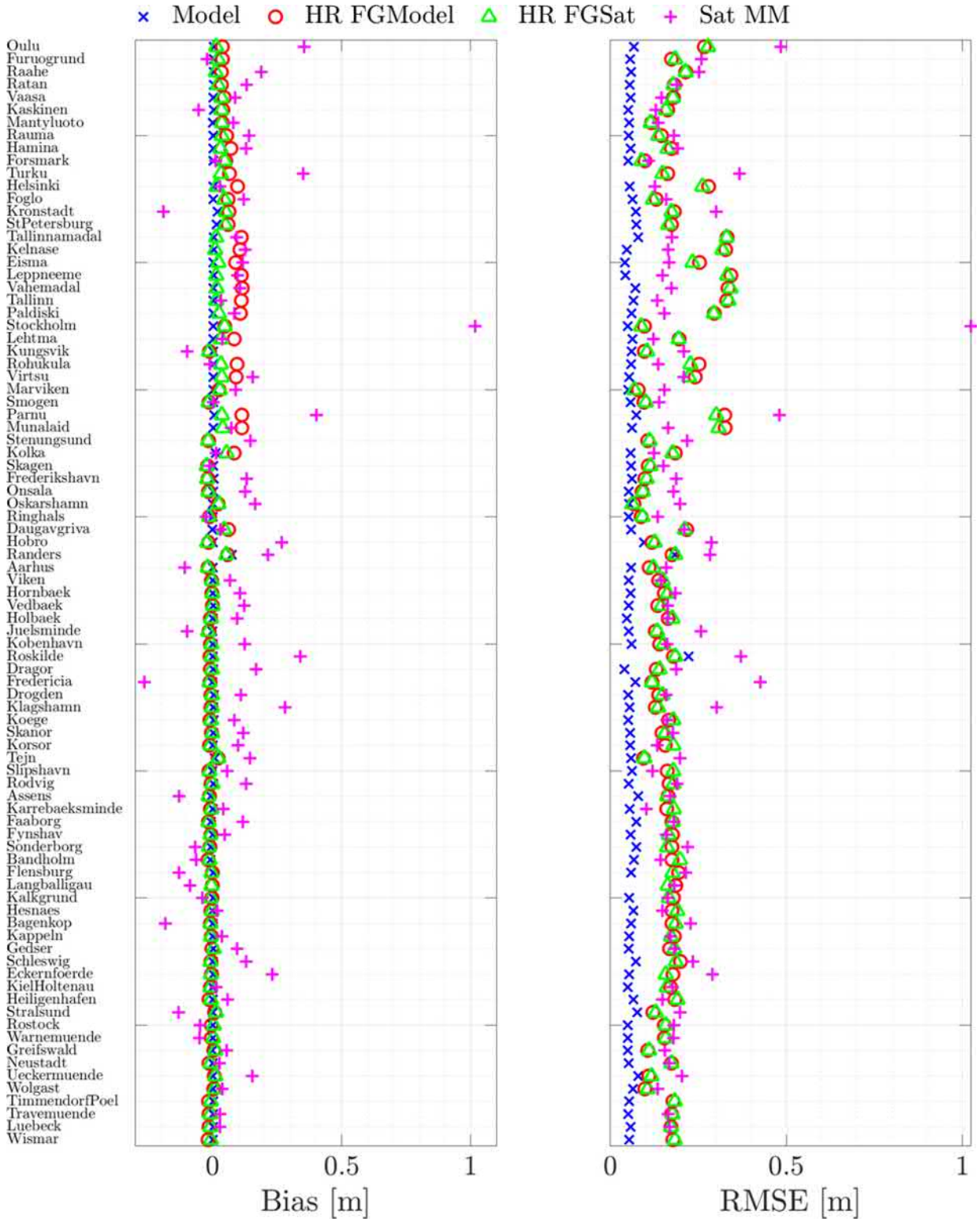

Figure 20. Bias (in m) and RMSE (in m) between the 3-day mean tide gauge observations and the model (blue cross), the FGModel (red circle), FGSat (green triangle) and MM (pink plus).

3.3 Identify and analyse extreme events

The ability of FGModel and FGSat to represent extreme sea level events and in particular the preconditions leading up to these events is investigated for a specific extreme sea level event in 2017. On January 4th and 5th in 2017 a surge event occurred in the western part of the Baltic Sea and in the Inner Danish Waters. This event was in Denmark named the Silent Storm Surge, as the

surge did not occur during a storm. In the days leading up to the event, there were continuous westerly winds pushing water into the Baltic Sea, thus building up water in the semi-enclosed sea (Figure 21, left). During the 4th and 5th of January the wind changed to a southern direction, pushing the build-up water out of the Baltic Sea and resulting in surges along the German coast and in the Inner Danish Waters (Figure 21, right).

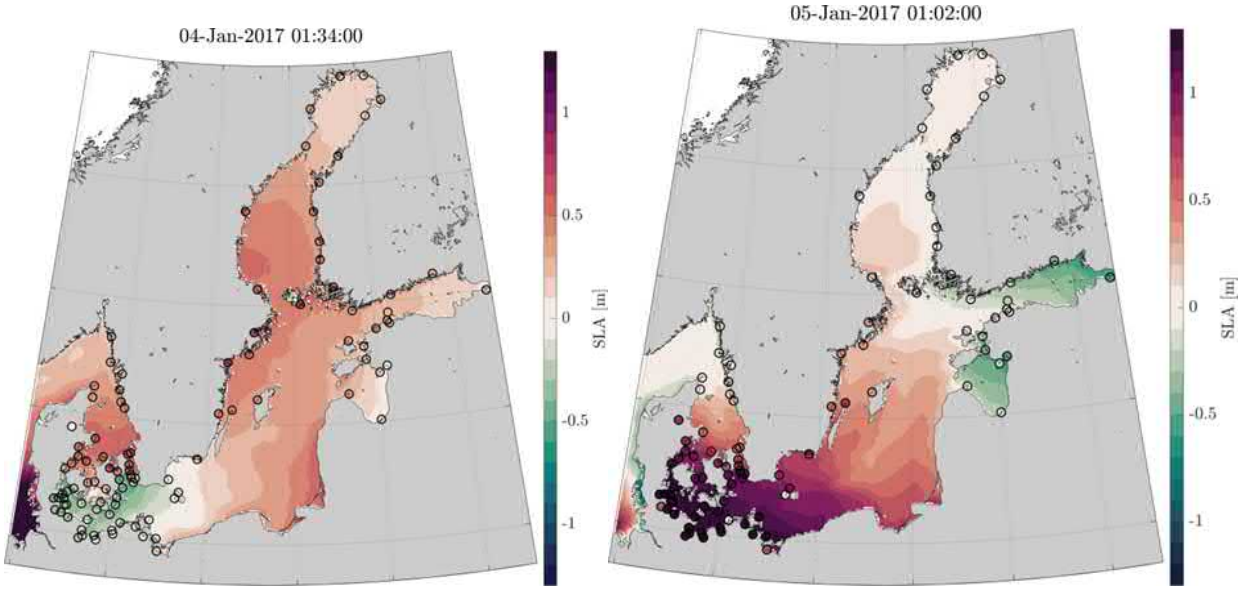

Figure 21. Sea level anomaly (SLA; in m) for the early hours of January 4th (left) and January 5th (right) for the storm surge model data (shading) and tide gauge observations (filled circles).

The time scale of extreme sea level events is shorter than the 3 days used to generate the HR gridded product. Hence, we did not expect to capture the extreme sea level event itself. Instead, we investigated if the HR gridded product can improve the preconditioning leading up to the event.

3.3.1 Preconditioning the Silent Storm Surge

As the HR gridded product are generated from 3-day averages, the preconditions for the Silent Storm Surge on January 5th are given by the average conditions from January 1st-3rd. The consequence of this is seen in Figure 22, showing the sea level anomaly at the Danish station Bagenkop for the different data types. Here, the high-temporal variability of the sea level and the inability to represent this by a 3-day average is illustrated by comparing the raw tide gauge observation (black line) to the 3-day average of this (black cross). The HR gridded products use the 3-day averages.

On top of the tide gauge observations are plotted the sea level anomaly for the storm surge model (blue), FGModel (red), FGSat (green) and the TUM MM (pink). For Bagenkop station, the sea level anomaly in FGModel and FGSat are higher than that in TUM MM, but still lower than the tide gauge observed 3-day mean sea level anomaly.

Expanding this comparison to all Validation stations, Figure 23 show the tide gauge observations on top of the two HR products (left column), the first guesses these are based on (middle column) and the 'product-to-beat', the TUM MM. The main feature to notice here is the discrepancies in the Inner Danish Waters and in particular in Kattegat between the tide gauge observed sea level anomalies and the HR gridded products. The cause of this is due to the intermittent occurrences of satellite tracks in this area. Satellites passed Kattegat 3 times during January 1st-3rd (on the 2nd at 2:45 and 8:36, in the 3rd at 2:12), during which there was negative or only slightly positive

sea level anomalies. The variable sea level in Kattegat during these 3 days is illustrated in Figure 18 showing the sea level anomaly for Ringhals. This highlights an additional issue with using 3-day averages: unless the satellite tracks are evenly distributed in time and space, they do not represent the average conditions.

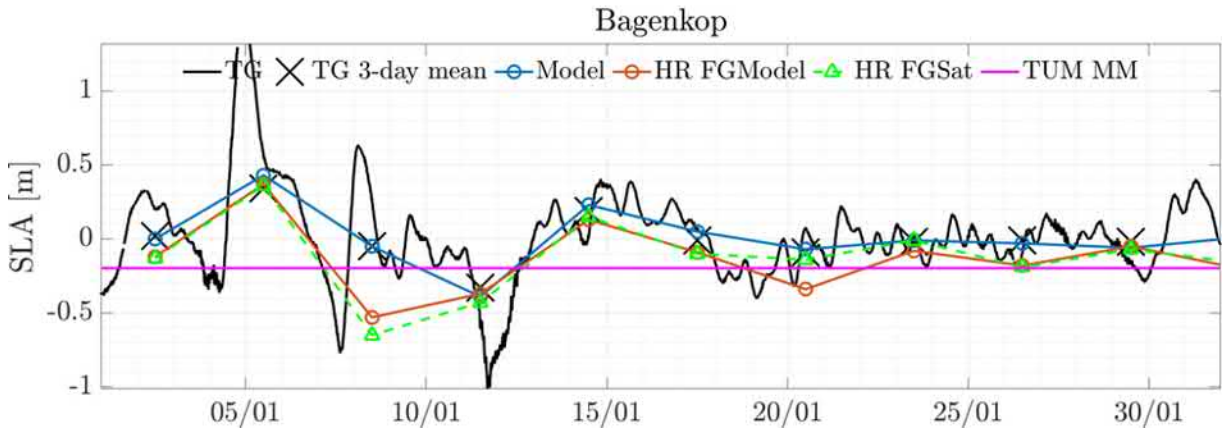

Figure 22. Sea level anomaly (SLA; in m) at Bagenkop for the raw tide gauge observation (black line), the 3-day mean of the tide gauge observation (black cross), the modelled sea level (blue circles), FGModel (red), FGSat (green) and the monthly mean altimetry product (TUM MM; pink).

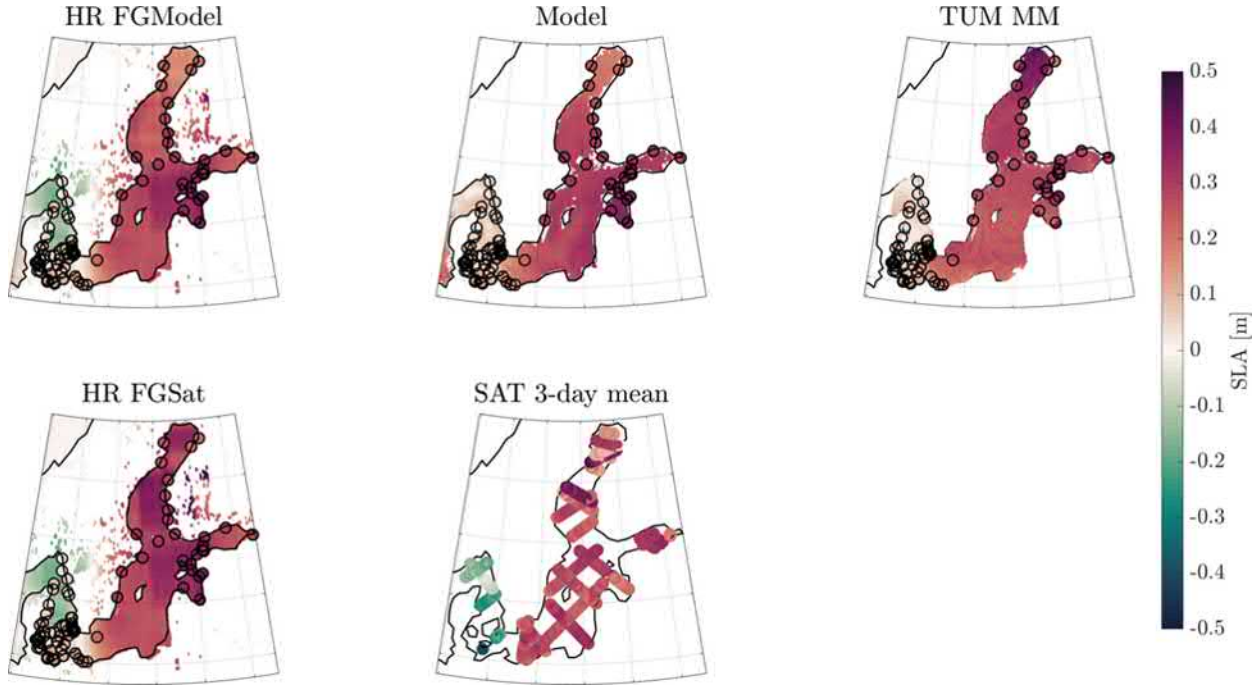

Figure 23. Sea Level Anomaly (SLA; in m). Shading shows the two HR products (left column), the First Guesses used (middle column) and the Monthly Mean Altimetry product (TUM MM; right column). 3-day mean tide gauge observations are laid on top in the filled circles.

3.4 Discussion and conclusion

We generated a 3-day mean sea level anomaly gridded product of the Baltic Sea using the DMI Optimal Interpolation (DMI-OI) method by combining satellite altimetry, tide gauge observations and error statistics from a storm surge model. Two versions of the HR product were generated: one where the previous 3-day analysis has been used as first guess and one, where the 3-day averaged model fields have been used. The value of these products was assessed by comparing them against the Baltic SEAL monthly mean altimetry product. The knowledge gained from the higher temporal resolution in our product (3-day mean compared to monthly mean) was clearly seen for most tide gauge stations, as both the bias and the RMSE was higher for TUM MM than for the two HR gridded products. Some areas in the Gulf of Finland, the Gulf of Riga and in the Inner Danish Waters showed artificially large and rapid sea level shifts in the HR products. The cause of these rapid shifts is most likely related to the insufficient spatial cover of satellite altimetry during the 3-day periods, but it is not clear yet and requires further analysis.

A potential use of this HR product is to improve the preconditions for storm surge simulations before extreme sea level events. This was assessed for a surge event in the western Baltic and Inner Danish Waters occurring on January 5th 2017, the Silent Storm Surge. Satellite altimetry only captures snapshots of the sea level and due to the high variability of sea level changes, this might not be representative of the entire 3 day period. This was the case for Kattegat in the example shown here.

A potential solution for this is to use a shorter temporal resolution of 1 day. This will result in a smaller spatial coverage, but it will capture the sea level variability better. Alternatively, the satellite altimetry data could be used ‘raw’, i.e. not averaged over it in time but only be used when and where it is.

Combining satellite altimetry with tide gauge observations on a high temporal resolution provides a reasonable representation of the Baltic Sea sea level. One advantage of this product is the independence from storm surge models and their associated error sources as one of the gridded products (FGSat) only uses the storm surge model error statistics. FGSat were in general very

similar to FGModel over the entire year. Additionally, the high-temporal resolution product and the TUM MM complement each other, as they are suited for different situations and analyzes, i.e. TUM MM is better suited for long-term sea level analysis. The HR gridded products will benefit from further analysis, exploring the ideas presented above.

4. Assessment of sea level variability (TUM)

4.1 Methodology for sea level analysis

4.1.1 Trend computation

We estimate the seasonal cycle, the linear trend and the parameter uncertainties by fitting multi-year monthly averages (to approximate the seasonality) and a linear trend to the data (least squares). The annual cycle amplitude is defined as one-half of the difference of the largest and the lowest monthly average (the annual cycle uncertainty is thus based on the combined uncertainty of these individual averages.) Trend uncertainties are derived while accounting for auto-correlated errors in the data using Maximum Likelihood Estimation (MLE). To identify the most appropriate noise model, we investigate the fit of a variety of different stochastic noise model combinations as done in e.g. Royston et al. (2018): These are an autoregressive AR(1) noise model, a power law plus white, a generalized Gauss Markov (GGM) plus white, a Flicker noise plus white and an auto-regressive fractionally-integrated moving-average (ARFIMA) model. We use the Hector software to fit the different noise models [Bos et al., (2019)]. For the considered domain we find that on average the AR(1) has the lowest mean (or median) values of the Akaike Information Criterion (AIC, Akaike (1998)) and the Bayesian Information Criterion (BIC, Schwarz (1978)). Thus, this model is selected to assess formal parameter uncertainties.

4.1.2 EOF Analysis

We perform a Principal Component Analysis (PCA) to investigate the major modes of SL variability in the BS. For this purpose, we consider a set of multiple SL anomalies $x_k(t)$, where k and t describe the dimensionality of the data in space and time, respectively. To identify the maximum modes of joint space and time variations, we determine a set of linear combinations in form of PCs $u_m(t)$ and associated eigenvectors or empirical orthogonal functions (EOFs) e_{km}. The linear combinations, or the modes are arranged such that the the higher-order modes $m = 1, 2, 3, \ldots$ explain the highest variance fractions of the data. The PCs $u_m(t)$ are equal to the projection of the data vector onto the mth eigenvector e_{km} (e.g. Wilks et al. (2006)):

$$u_m(t) = \sum_{k=1}^{K} e_{km} x_k(t), \quad m = 1, \ldots, M \tag{4}$$

In this manner the data is explained by a set of PCs, which represent time series (which are uncorrelated or independent from each other), as well as the EOFs (or eigenvectors) which represent the geographical coherence of the individual modes.

We compute the EOF and their PC from monthly gridded de-seasoned SL. The latter is called SLA in this description, since it is the anomaly with respect to a monthly-based average (for example, based on the average for all Januarys in the period of record at a particular grid point). In this way we capture the 'full-year' monthly variability and no seasonal variations. Because monthly SL variability is generally most pronounced in winter, the derived full year EOF-pattern are very similar to the once derived only over the winter season (DJF). EOF patterns are given as point-

wise correlations of their PCs with SLAs. We use the python distribution EOFs Dawson (2016) for computation of the EOF.

4.1.3 Regression Analysis

We use a simple statistical approach to understand the relation of surface winds and SL trends: We compute point-wise linear regressions of the deseasoned, monthly and basin-averaged surface winds (horizontal U component and vertical V component) and SLAs by solving for: $SLA(t) = aU(t) + bV(t) + \eta$ (e.g. Dangendorf et al. (2013), Storch and Zwiers (1999)). Based on these point-wise linear regressions we estimate a linear trend (without seasonal component) which is explained by the individual wind components as well as the explained variance of SL variability by the components (as for example in Dangendorf et al. (2013)).

4.2 Results

Figure 24 shows the map of sea level trends computed using our dataset. Superimposed in circles along the coast are the estimations of the TGs. TG estimates are corrected for the Glacial Isostatic Adjustment. In accordance to previous studies based on the altimetry era, it is found that the absolute sea level has been rising throughout the region. The rate of sea level rise increases from the Arkona Basin to the Baltic Proper, and from the Baltic Proper to the Bothnian Bay. While such a pattern has been previously observed, the added value of our analysis is the insight on the spatial variation of sea level trends observed seamless from the proximity of the coast to the open ocean, which was lacking or limited in the recent literature based on observations [Gräwe et al. (2019)].

By retrieving the sea level information from the leads among sea ice in winter, we are able to extend the analysis to areas characterised by seasonal sea ice coverage, i.e. Gulf of Bothnia and Gulf of Finland. Nevertheless, gaps are still present in such regions along the coast. Other remaining gaps involve locations in the Danish Archipelago, where the predominant presence of land within the search radius of each grid point hinders the possibility to find enough data in particular during years in which few altimeters were flying. Finally, our sea level analysis does not provide results in some parts of the Turku Archipelago (south-western Finnish coast), since the over 40000 islands that form this region are such that the vast majority of sea level retrieval would be affected by land contamination at distances of hundreds of meters, which is well below the possibilities of any LRM altimeter, even using a coastal retracking.

These data gaps could be artificially adjusted by means of heavier interpolation and different weighting in the grid process, nevertheless the choice in this study was to avoid generating information that is indeed not available. The comparison of the agreement between the sea level trends from different altimetry dataset and TGs presented in Figure 25 is a proof of the validity of our compromise. In the histograms, the sea level trend estimates from the TGs are compared with the closest estimates from altimetry using data from this study (panel a), data from Copernicus Marine Environment Monitoring Service (panel b, [Taburet el al. (2019)]). In panel c, the length of the time series of this study is 1995–2015, to enable the comparison with the gridded product of the Sea Level Climate Change Initiative (panel c, SLCCI [Legeais et al. (2018)]). For the latter comparison, the years considered were 1995–2015, to match the availability of SLCCI. In both pairs of comparison, the comparability between trends from altimetry and from tide gauges improves by 9% using the Baltic+ data in terms of root mean square of the differences. All the altimetry dataset show a median of the trends that is about 0.2 mm/yr lower than in the TG records.

Figure 24b also shows the uncertainty of the computed trends. This is a purely statistical function of the amount of along-track sea level estimations within a grid point and their variability, taking in consideration the serial correlation. The same method is used also to estimate the uncertainty of the trend estimated from TGs, which also do not have an uncertainty value associated to each measurement. This is in line with most of the studies estimating trends from altimetry measurements, for example [Benveniste et al. (2020)]. The possibility to associate an uncertainty to the single altimetry measurement has been explored by [Ablain et al. (2016)] and analysed in the Baltic Sea by [Madsen et al. (2019)], but requires a large amount of assumptions concerning every single correction added to the altimetric range. Nevertheless, our statistical uncertainties show a similar pattern and range of the ones shown in [Madsen et al. (2019)].

By grouping the grid points according to their location, Figure 26 displays the averaged sea level trends of each sub-basin with their statistical uncertainty. The rise in sea level is statistically significant in all sub-basins. The spatial variation of the best estimate of the linear trend is confirmed, although the uncertainties due to the larger variability of the sea level time series in most of the sub-basins cannot ensure statistical significance to this assertion yet.

Figure 27 shows the trends in sea level considering only the winter months (panels a,c) and only the summer months (panels b,d). Positive trends are found in the winter sea level, with a difference of over 4 mm/year comparing the winter trend in their minimum and maximum values. A similar gradient in sea level trend estimates is seen for the full time series in Figure 24b. This spatial variation in the trend is less pronounced in summer. Since these assertions are only based on the best estimates, given the high statistical uncertainties, we further investigate the tide gauge records, which also spans much longer periods than the altimetry time series.

Indeed, the same gradient of about 4 mm/yr in sea level trend estimates from altimetry across the basin is observed in the most recent TG record (Figure 28a). Figure 28a-d report the best estimate of the linear trends in sea level from the longest TG time series in the region, spanning from 1920 to 2020 at intervals of 25 years. It is observed that not only a rise in sea level is marked in the last 50 years, but also that the gradient between south-west and north-east of the basin has been increasing in time.

It is worth to discuss the possible reason of such a pattern. The altimetry dataset, despite shorter than some TGs records in the area, provides the necessary spatial coverage for this and is further analysed in the next section.

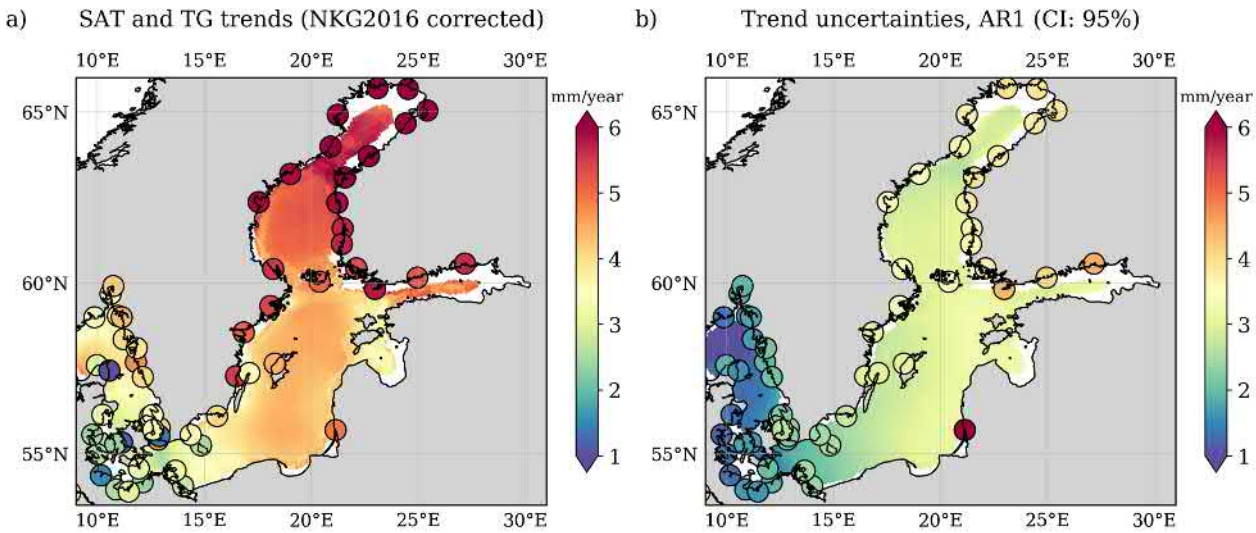

Figure 24. Sea level trends (a) and corresponding uncertainties (b) estimated by altimetry (grid points) and tide gauges (circles) from May 1995 to May 2018. Tide gauges are corrected for the Glacial Isostatic Adjustment using the NKG2016 model. Uncertainties are reported as 95% confidence interval.

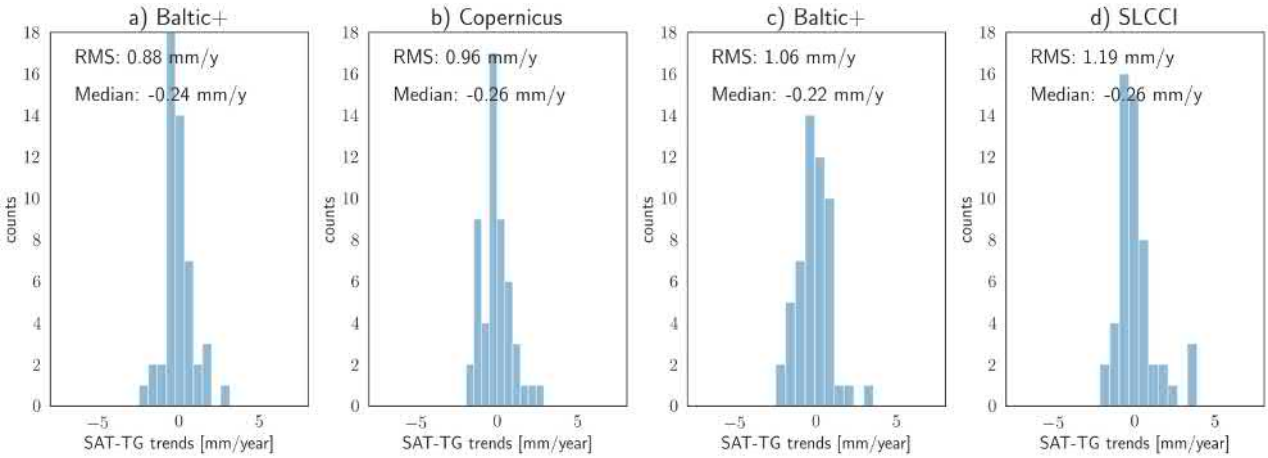

Figure 25. Histograms of the differences in estimated sea level trends from gridded altimetry (SAT) and tide gauges (TG), compared using the closest point. Each panel correspond to different SAT dataset: the altimetry dataset from May 1995 to May 2018 developed in this study (panel a, Baltic+), the altimetry dataset from May 1995 to May 2018 CMEMS (panel b, Copernicus), the altimetry dataset from May 1995 to December 2015 developed in this study (panel c, Baltic+), the altimetry dataset from May 1995 to December 2015 of the Sea Level Climate Change Initiative (panel d, SLCCI)

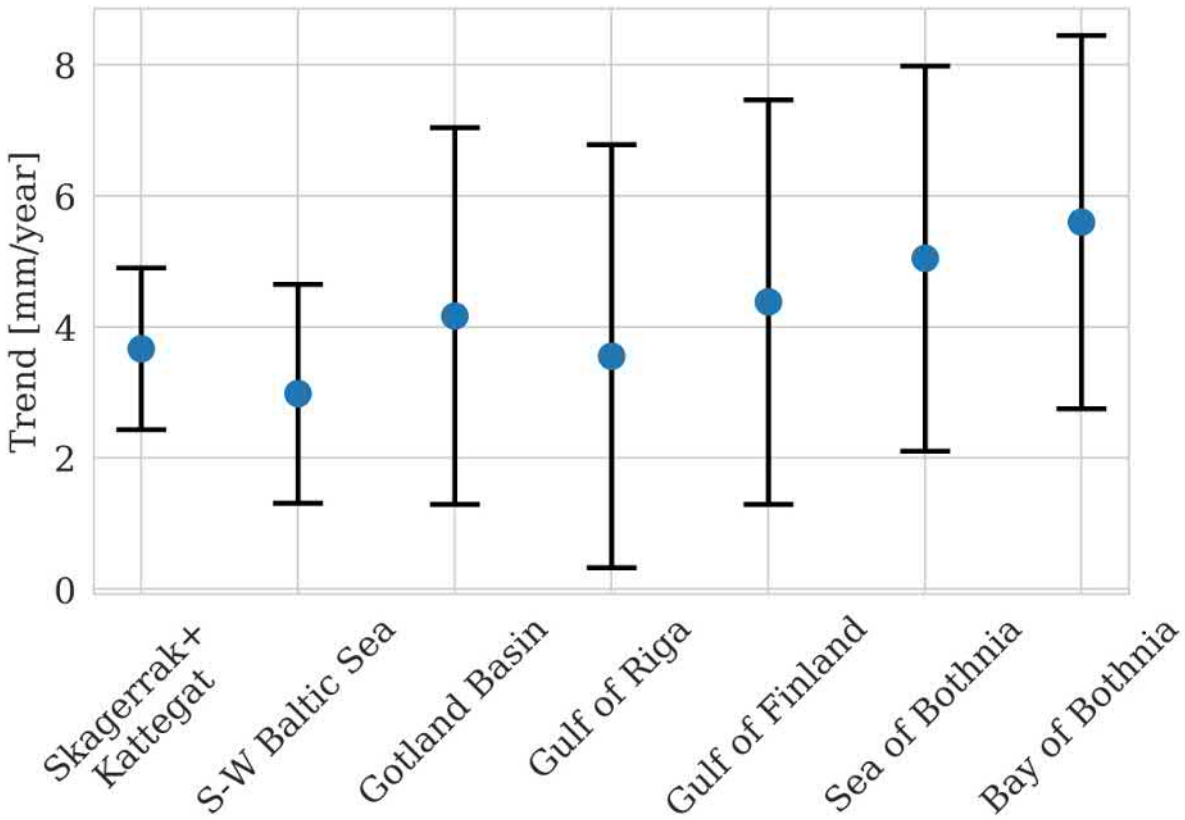

Figure 26. Sea level trends from gridded altimetry averaged across different subbasins of the Baltic Sea from May 2015 to May 2018. Corresponding uncertainties are reported as black error bars.

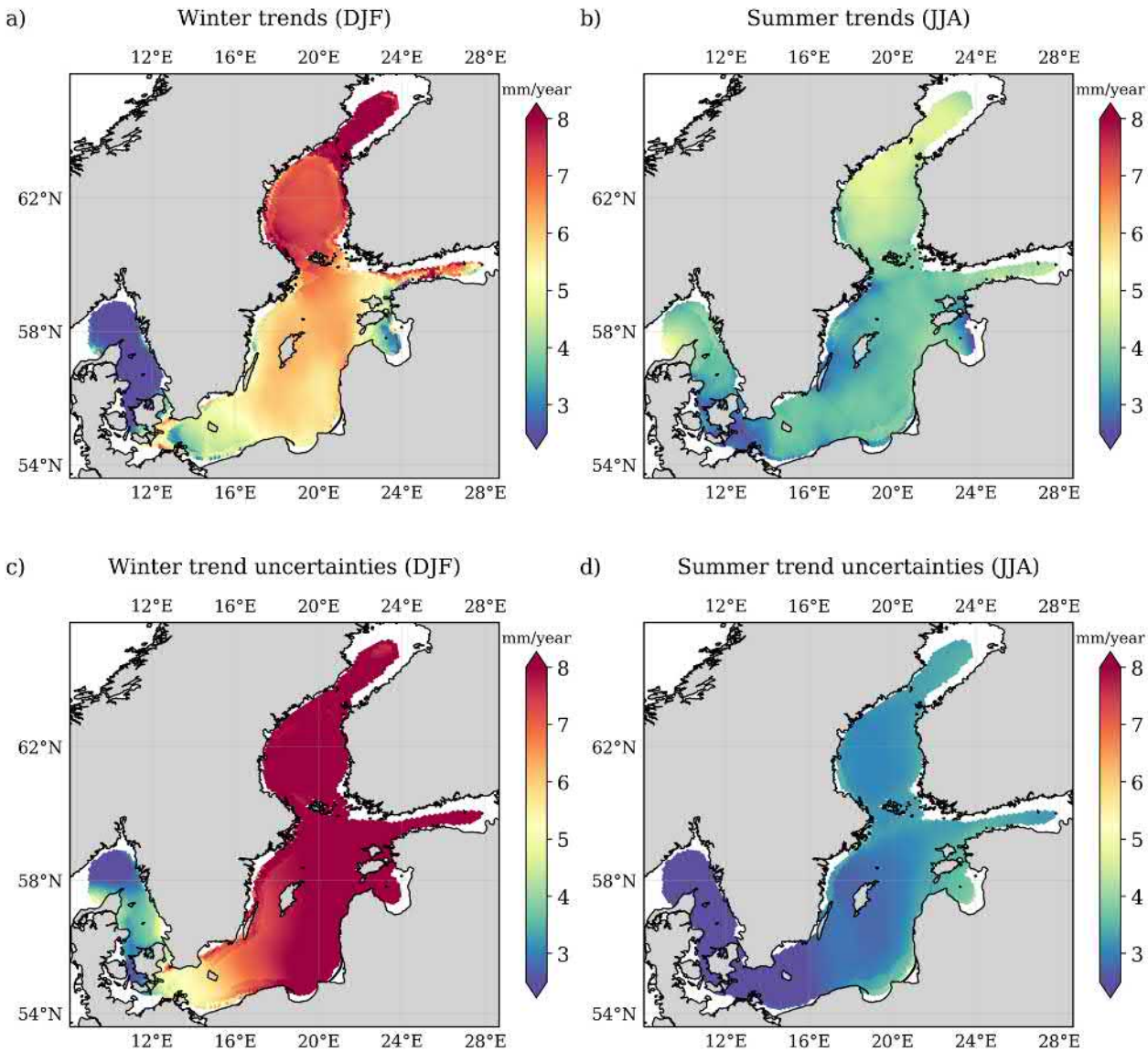

Figure 27. Sea level trends with uncertainties from gridded altimetry computed using only the winter months (December, January and February, panels a and c) and the summer months (June, July and August, panels b and d).

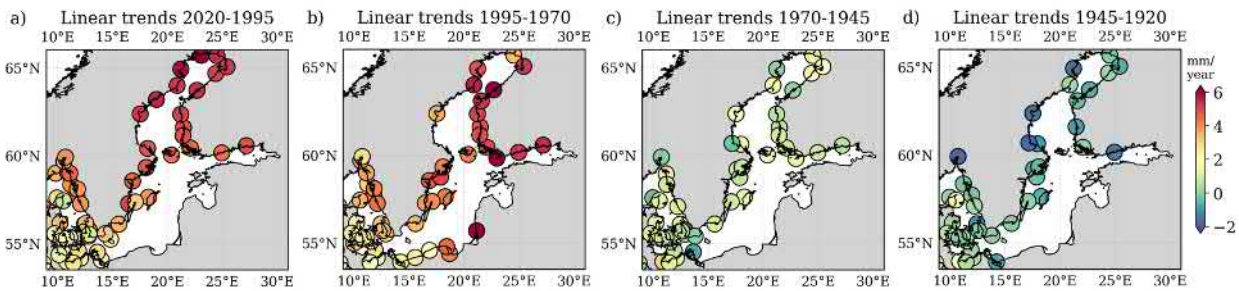

Figure 28. Sea level trends from tide gauges computed at 25-year intervals from 1945 to 2020.

4.2.1 Relationships with wind pattern

To analyse the spatial and temporal pattern of sea level variability and how they differ locally across the basin, we perform an EOF analysis on the deseasoned time series at each grid point. Figure 29, panels a and d, shows the spatial patterns of the first and second EOFs. We find that 87.4% of the variance in the whole domain is driven by the first EOF, which represents a sea level anomalies of the same sign all across the basin. The second EOF, while representing 3.1% of the variance, drives a sea level variability with a strong gradient between South-West and North North-East of the basin, generating sea level anomalies of opposite sign.

To characterise these two modes, we correlate the accompanying principal components (PCs) to the horizontal (U) and vertical (V) components of the surface wind from the ERA5 reanalyses [Hersbach et al. (2020)]. The results displayed in Figure 29, panels b,c,e,f, show that the PC1 is correlated with U in the South-West of the basin, with the correlation degrading towards North. The predominance of the zonal component in shaping the sea level variance of the region is in accordance with previous studies, for example [Johansson et al. (2014)]. PC2 is instead well described by the variability of V, with correlation values over 0.5 in all our region of study.

The wind variability affect differences in sea level across the basin, which may affect the local estimates of linear trend during the altimetry era. To further study this mechanism, we perform a multiple regression analysis of the sea level time series using the U and V component. The results are shown in Figure 30, in which the explained trend for each component of the wind and for the sum of the two components is presented, with its uncertainty. While the regression using U does not show a trend all across the basin, V is responsible for a gradient of over 1 mm/yr from South to North. Although a conclusive statement with statistical relevance cannot be drawn, given the uncertainties, both EOF and regression analysis point out to the same role of the vertical wind component to shape a North-South imbalance in the sea level anomalies.

Recently, spatial gradients of the sea level trend within the Baltic Sea have been attributed, based on circulation models, to an increase in the days of westerly winds, which increase transport towards the east [Gräwe et al. (2019)]. Our observational evidence suggests that the meridional component plays also a role in shaping the differences between North North-East and South-West of the basin.

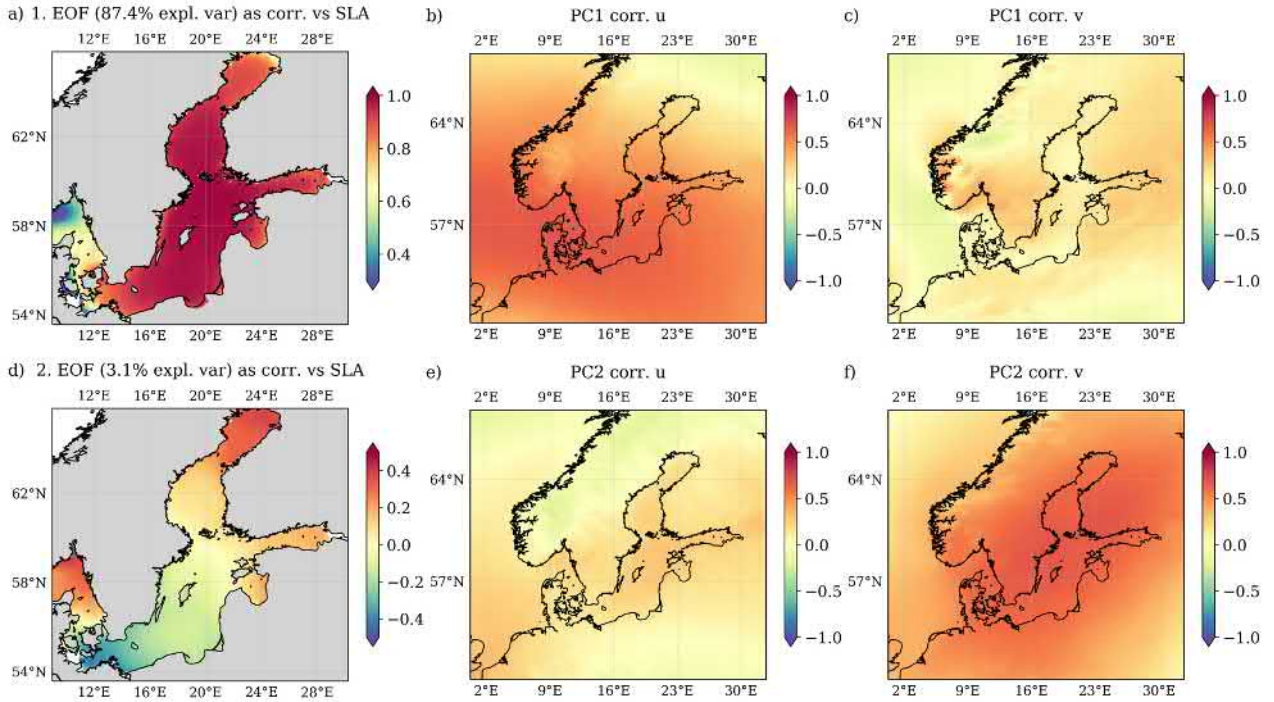

Figure 29. Panels a and e: empirical orthogonal functions of sea level variability expressed as correlation of their corresponding principal component against the sea level time series at each grid point. Panels b and c: correlation between the first principal component of sea level variability and the horizontal (u) and vertical (v) component of the surface winds. Panels d and e: same for the second principal component.

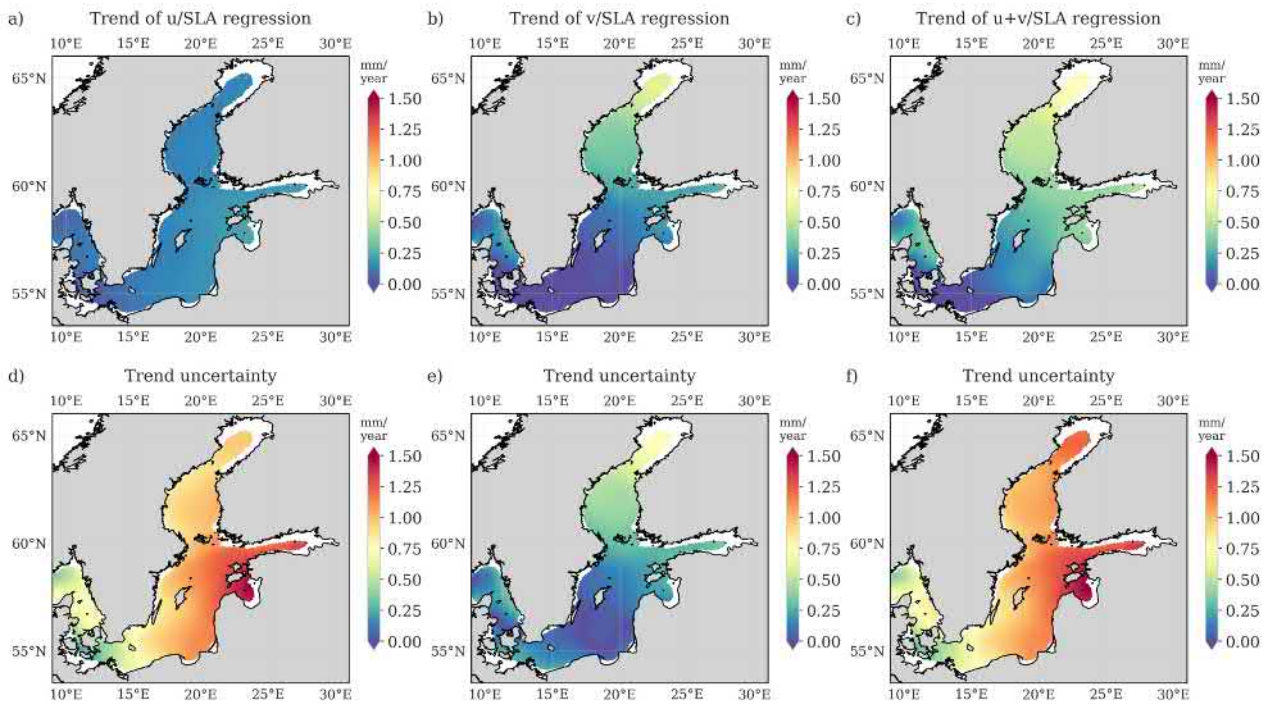

Figure 30.
Trends (and corresponding uncertainties) resulting from the regression of the horizontal (U,

panel a) and vertical (V, panel b) component of the surface winds on the SL time series. Panel c shows the trend obtained summing the two components of the regression.

4.2.2 Relationships with North-Atlantic oscillation

The large scale variability of both sea level and wind patterns in our area of study can be well described using climate indeces. There is a strong agreement that the North Atlantic Oscillation (NAO) is the leading mode of atmospheric circulation in the region [Andersson (2002), Jevrejeva et al. (2005)]. Interconnections with other indeces have been shown to play a role in the area, such as the East Atlantic pattern (EAP), Scandinavian (SCAN) pattern [Chafik et al. (2017)] and the Baltic Sea and North Sea Oscillation index (BANOS) [Karabil et al. (2018)].

We focus on the local effects of NAO variability, since the relationship of NAO to the Baltic sea level variability has been previously reported to be spatially heterogeneous and characterized by a significant increase from west to east ([Jevrejeva et al. (2005)] with TG observations, [Stephenson et al. (2006)] with global models). Figure 31a shows that in the altimetry era the correlation between the sea level variability and the NAO index is dominant in winter, as expected, and uniform in all domain except for the South West.

The possibility given by our dataset to observe local sea level changes in winter in the sea-ice covered areas allow a basin-wide comparison of the Bay of Bothnia against the South West, which present the largest discrepancies in the linear trend estimations. In Figure 31b the difference in sea level (Bay of Bothnia - South West) in the winter months is plotted against the NAO index. The correlation between the two curves is 0.71%. From the comparison it is evident that positive NAO phases maintain an imbalance between the anomalies in the two basins, which is reversed when the NAO phase is negative. The intensity of the NAO phase, which is linked to the local wind forcing [Dangendorf et al. (2013)], is here shown to drive differences of sea level anomaly at a sub-basin scale in the Baltic Sea, with inter-annual variations that have an effect on the linear trend of the sea level estimated on a 20-year long time series.

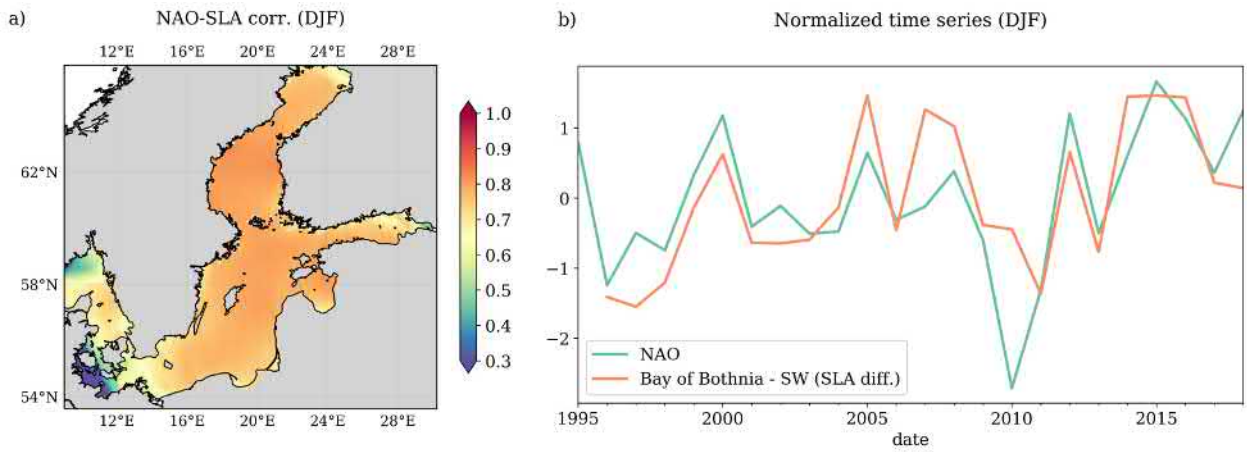

Figure 31. Panel a: correlation of the North Atlantic Oscillation index with sea level from gridded altimetry. Panel b: normalised time series of North Atlantic Oscillation index (green) and sea level

difference between Bay of Bothnia and SW subbasins (orange). Each point represents the time average of the quantities of the winter months December, January and February.

Winds affect surface circulation of water masses through Ekman transport. We show in Figure 32 the average winter wind speed direction (panels e to h) and the resultant Ekman currents (panels a to d) in selected examples to observe the mechanism that may regulate the sea level differences among different sub-basins within the Baltic Sea, based on the years of high and low differences between the winter SLAs of Bay of Bothnia and the South West as reported in Figure 31b. We analyse the Ekman transport at 15 m from GlobCurrent [Rio et al. (2014)]. The Ekman currents are distributed on a 1/4 of a degree grid and they are derived using wind stress from ECMWF, Argo floaters and drifter data.

When considering these results, we are dropping the hypothesis of a fully developed Ekman spiral, in which case the transport would be perpendicular to the wind direction. Nevertheless, given the low depths of the South West of the Baltic Sea, the 15-depth Ekman transport should be a good approximation at least in this subbasin. Since Bothnia is partially covered by sea-ice for most of the winters, which hinders formation of an Ekman spiral, and since sea-ice is not taken into account in the GlobCurrent product, we are mostly interested in the effect of the Ekman currents in the southern part of the domain. Results are consistent, when the wind speed is relevant, with the Ekman transport pushing the surface waters to the right of the wind direction.

Winters with SLA higher in Bothnia than in South West (e.g. 2000, 2014) are either characterised by strong westerlies in South West whose intensity decrease towards the North (e.g. 2000), and/or my a marked southerly component of the wind (e.g. 2014). Years were the differences are very low, or even flip (e.g. 1996, 2010) are often characterised by much lower wind speed.

The easterlies and north easterlies winds are seen in the Ekman currents to displace water away from the South West towards the East. Ekman currents are much lower towards the north, moreover the Bay of Bothnia is at least partially covered by sea ice for most of the winter months, hindering most of the local Ekman-related effect. The years where the sea level anomalies are lower, the Ekman transport away from the South West drops significantly, and it is in some cases reverses (as in 2010), during the strongest negative phase of winter NAO.

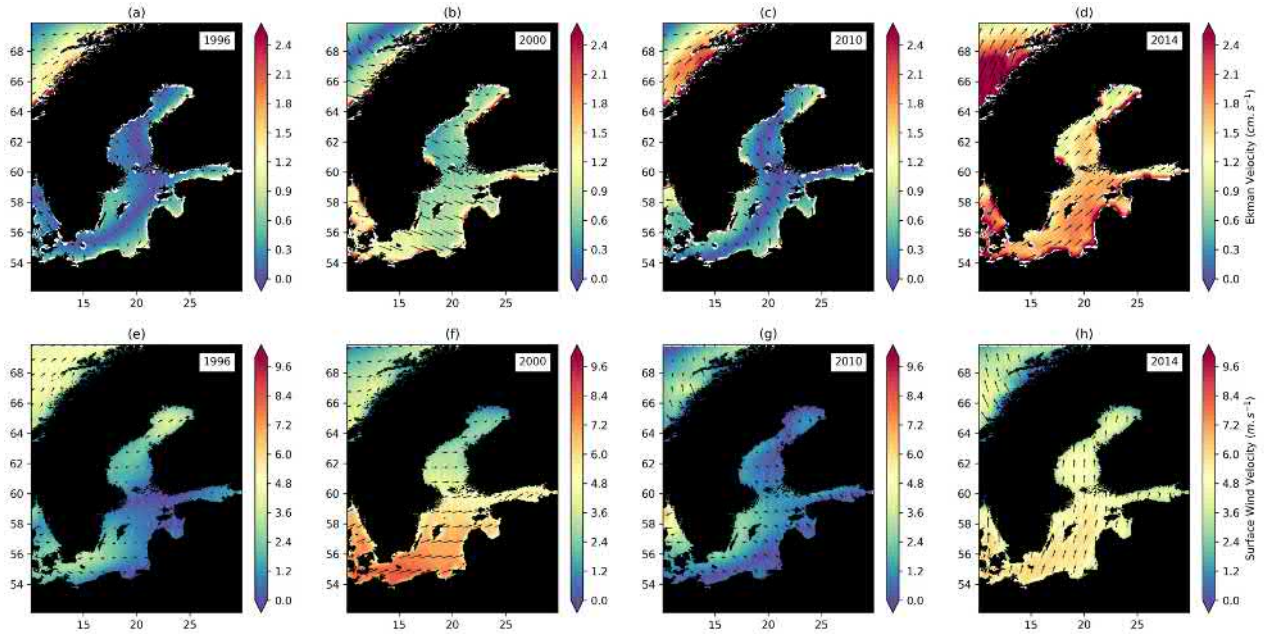

Figure 32. Velocity of the Ekman currents (panels a-d) and surface wind velocity (panels e-h) during the winters of four selected years. The arrows represent the direction of the velocity vectors and are scaled according to their magnitude.

5 Assessment of vertical land motion from altimetry and relative sea level trends (FMI)

5.1 Data and methods

The land uplift due to the postglacial rebound has been estimated from the relative sea level (RSL) trends of tide gauge data. In the Baltic Sea region, there are over 100-year long datasets from many tide gauges. The land uplift causes a negative linear trend in the tide gauge measurement, as the relative mean sea level decreases due to the vertical land motion.

The altimeter datasets are already 25 years long, making it possible to determine also absolute sea level (ASL) trends. As the altimetry measurement of the satellite is not affected by the uplift of the Earth's crust, it is possible to determine the vertical land motion (VLM) from the difference of absolute and relative sea level trends

$$VLM = ASL - RSL \tag{5}$$

The land uplift can be nowadays also be evaluated directly by GPS stations, measuring the horizontal and vertical land motion. For the locations of the GPS stations in the Baltic Sea with enough data (Class A) to determine the vertical trend, see Fig. 12 in Dataset Description, Deliverable D2.1.

For the determination of absolute sea level trends, we combined the along-track data of all missions and used the data from the point closest to the tide gauge with good quality (distance less than 20 km) to create the altimeter dataset for each tide gauge. Trends were calculated from linear fits to the altimeter and tide gauge data 1995-2019. Finally the results were compared with the NKG2016LU land uplift model by [Vestøl et al. (2019)]

5.2 Results

There were altogether 111 tide gauges with more than 100 data points in the combined along-track data 1995-2019 within 20 km distance from the tide gauge. For these tide gauges, we calculated trends for the along-track and tide gauge data, representing the absolute and relative sea level trends. Figure 33 shows these trends in a map.

We attempted an estimation of the vertical land motion given by the difference of these trends. It turned out that there is a large variation in the along-track absolute sea level trends that makes is difficult to accurately determine the vertical land motion. The absolute trends vary from - 21 mm/yr to 26 mm/yr, having considerably larger variation than the absolute trends determined from the gridded dataset (see Figure 24 in Section 4). The relative sea level trends from tide gauge data have smaller spatial variation between tide gauges, and negative trends are observed in the northern Baltic Sea where the land uplift is largest.

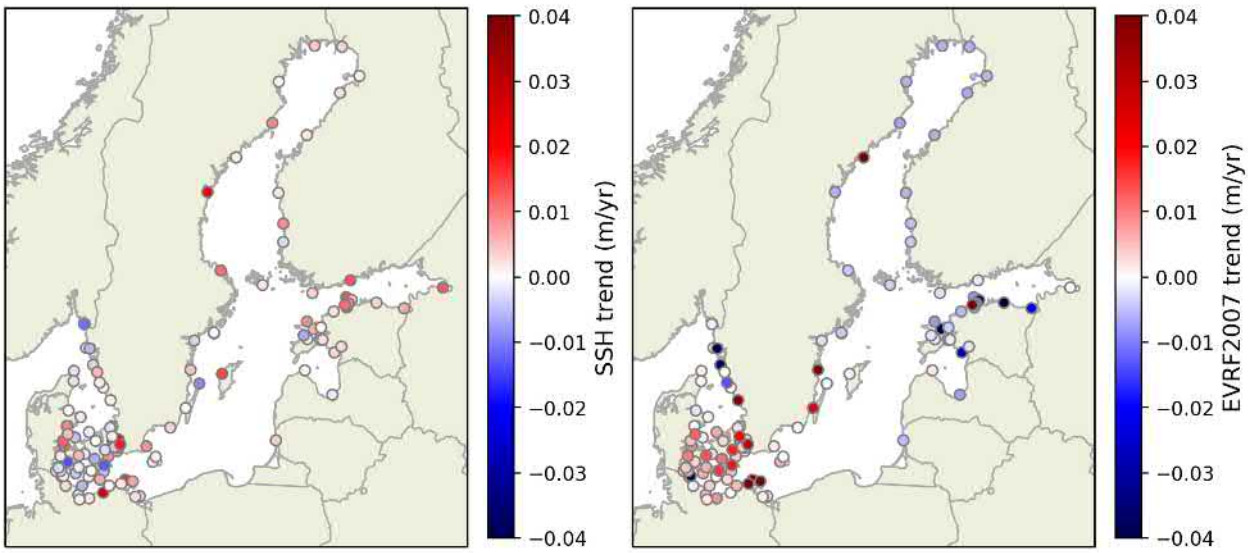

Figure 33. Absolute sea level trends from along-track data (left) and relative sea level trends from tide gauge data (right)

The values of the vertical land motion, obtained from the difference of trends, vary between -64 mm/yr to 59 mm/yr. The land uplift values given by NKG2016LU model are from 0 mm/yr to 11 mm/yr in the Baltic Sea region. Only 37 of the 111 tide gauges have VLM values within this range. The most reasonable values of VLM computed by differentiating tide gauges and altimetry were found in the Gulf of Bothnia, in particular at Kalix (10.6 mm/yr), Kemi (9.7 mm/yr), Furuögrund (7.0 mm/yr) and Kaskinen (7.9 mm/yr).

The difficulties in the determination of absolute trends were due to many factors. Even if overall we have altimeter data for 24 years, there are less than 1000 data points or only a couple of years of data available for many TGs. The natural variability of Baltic Sea level, over three meters for some TGs and long time intervals (especially in the earlier years) in the altimeter data cause large fluctuations in the altimeter data series, weakening the accuracy in the trend determination. In the southern Baltic Sea the land uplift is less than 2 mm/yr according to NKG2016LU model, and there the estimation of VLM from altimeter and TG trends would need more data to have values close to model values. One of the problems observed was due to the lower quality of ERS-2 coastal

retrievals compared to more modern missions. In comparison to tide gauges, ERS-2 along-track data were found to be biased low, leading to higher altimeter trends in the combined along-track altimeter dataset.

To summarize the results, the along-track data in the vicinity of the tide gauges was found to have large variations and in many cases small amount of data (less than 1000 SSH values) that hinder accurate determination of altimeter trends. As the frequency of the altimeter data for the past 10 years is higher, future updates using recent data will enable to better assess vertical land motion from altimeter and tide gauge data. It shall be noticed that this activity was experimental and not associated with the main objectives and deliverables of the project. Moreover, this exercise was based on simple assessment of trends using one single altimetry track coupled with the closest tide gauge. Future efforts shall aim at increasing the comparability and the length of the time series by matching multiple altimetry tracks. This could be achieved by identifying a wider area characterised by similar sea level variability, rather than limiting the analysis to the closest 20 km.

6 References

M. Ablain, J. Legeais, P. Prandi, M. Marcos, L. Fenoglio-Marc, H. Dieng, J. Benveniste, and A. Cazenave. Satellite altimetry-based sea level at global and regional scales. Surveys in Geophysics, pages 1–25, 2016. doi: 10.1007/s10712-016-9389-8.

H. Akaike.Information Theory and an Extension of the Maximum Likelihood Principle, pages199–213. Springer New York, New York, NY, 1998. ISBN 978-1-4612-1694-0. doi: 10.1007/978-1-4612-1694-015.

Andersen, O. B., Stenseng, L., Piccioni, G., & Knudsen, P. (2016). The DTU15 MSS (Mean Sea Surface) and DTU15LAT (Lowest Astronomical Tide) reference surface. Paper presented at the ESA Living planet symposium 2016, Prague, Czech Republic. Retrieved from ftp.space.dtu.dk/pub/DTU15/DOCUMENTS/MSS/DTU15MSS+LAT.pdf

H. C. Andersson. Influence of long-term regional and large-scale atmospheric circulation on the Baltic sea level. Tellus A: Dynamic Meteorology and Oceanography, 54(1):76–88, 2002.

J. Benveniste, F. Birol, F. Calafat, A. Cazenave, H. Dieng, Y. Gouzenes, J. Legeais, F. Leger, F. Nin˜o, M. Passaro, C. Schwatke, and A. T. C. C. I. C. S. L. T. Shaw. Coastal sea level anomalies and associated trends from jason satellite altimetry over 2002–2018. Scientific Data, 7, 2020. doi: 10.1038/s41597-020-00694-w.

M. Bos, R. Fernandes, and L. Bastos. Hector user manual version 1.7. 2.available from http://segal.ubi.pt/hector/, 2019.

Brown, G. S., The average impulse response of a rough surface and its applications, IEEE Transactions on Antennas and Propagation, 25 (1977), pp. 67-74

L. Chafik, J. E. Ø. Nilsen, and S. Dangendorf. Impact of North Atlantic teleconnection patterns on northern European sea level. Journal of Marine Science and Engineering, 5(3):43, 2017. doi: https://doi.org/10.3390/jmse5030043.

S. Dangendorf, C. Mudersbach, T. Wahl, and J. Jensen. Characteristics of intra-, inter-annual and decadal sea-level variability and the role of meteorological forcing: the long record of Cuxhaven. Ocean Dynamics, 63(2-3):209–224, 2013. doi: https://doi.org/10.1007/s10236-013-0598-0.

A. Dawson. eofs: A library for eof analysis of meteorological, oceanographic, and climate data. Journal of Open Research Software, 4(1), 2016. doi: http://doi.org/10.5334/jors.122.

Forsberg, R. (1991), A new high-resolution geoid of the nordic area, in Determination of the geoid, pp. 241–250, Springer.

U. Gräwe, K. Klingbeil, J. Kelln, and S. Dangendorf. Decomposing mean sea level rise in a semi-enclosed basin, the baltic sea. Journal of Climate, 32(11):3089–3108, 2019. doi: https://doi.org/10. 1175/JCLI-D-18-0174.1.

Høyer, J. L., & Karagali, I. (2016). Sea surface temperature climate data record for the North Sea and Baltic Sea. Journal of Climate, 29(7), 2529-2541.

H. Hersbach, B. Bell, P. Berrisford, S. Hirahara, A. Hor´anyi, J. Munoz-Sabater, J. Nicolas, C. Peubey, R. Radu, D. Schepers, A. Simmons, C. Soci, S. Abdalla, X. Abellan, G. Balsamo, P. Bechtold, G. Biavati, J. Bidlot, M. Bonavita, G. De Chiara, P. Dahlgren, D. Dee, M. Dia- mantakis, R. Dragani, J. Flemming, R. Forbes, M. Fuentes, A. Geer, L. Haimberger, S. Healy, R. J. Hogan, E. H´olm, M. Janiskov´a, S. Keeley, P. Laloyaux, P. Lopez, C. Lupu, G. Radnoti, P. de Rosnay, I. Rozum, F. Vamborg, S. Villaume, and J.-N. Thepaut. The ERA5 global reanalysis. Quarterly Journal of the Royal Meteorological Society, 2020. doi: 10.1002/qj.3803. URL https://rmets.onlinelibrary.wiley.com/doi/abs/10.1002/qj.3803.

S. Jevrejeva, J. Moore, P. Woodworth, and A. Grinsted. Influence of large-scale atmospheric circulation on european sea level: results based on the wavelet transform method. Tellus a: Dynamic Meteorology and Oceanography, 57(2):183–193, 2005.

M. M. Johansson, H. Pellikka, K. K. Kahma, and K. Ruosteenoja. Global sea level rise scenarios adapted to the Finnish coast. Journal of Marine Systems, 129:35–46, 2014. doi: https://doi.org/10. 1016/j.jmarsys.2012.08.007.

S. Karabil, E. Zorita, and B. Hünicke. Contribution of atmospheric circulation to recent off-shore sea-level variations in the baltic sea and the north sea. Earth System Dynamics, 9:69–90, 2018. doi: 10.5194/esd-9-69-2018.

Knudsen P, Brovelli M. Collinear and cross-over adjustment of Geosat ERM and Seasat altimeter data in the Mediterranean Sea. Surveys in geophysics. 1993; 14(4-5):449–459.

J.-F. Legeais, M. Ablain, L. Zawadzki, H. Zuo, J. A. Johannessen, M. G. Scharffenberg, L. Fenoglio- Marc, M. J. Fernandes, O. B. Andersen, S. Rudenko, et al. An improved and homogeneous altimeter sea level record from the esa climate change initiative. Earth System Science Data, 10(1):281, 2018.

K. S. Madsen, J. L. Høyer, Ü.. Suursaar, J. She, and P. Knudsen. Sea level trends and variability of the baltic sea from 2d statistical reconstruction and altimetry. Frontiers in Earth Science, 7:243, 2019. doi: https://doi.org/10.3389/feart.2019.00243.

M. Rio, J.-F. Piolle', J. J.A., and C. Donlon. GlobCurrent product format and content. European Space Agency, available from http://globcurrent.ifremer.fr/products-data/products-overview, accessed on 10/11/2020, 2014.

S. Royston, C. S. Watson, B. Legresy, M. A. King, J. A. Church, and M. S. Bos. Sea-level trend uncertainty with Pacific climatic variability and temporally-correlated noise.Journal of Geophysical Research: Oceans, 123(3):1978–1993, 2018. doi: 10.1002/2017JC01365.

Scharroo, R., E. Leuliette, J. Lillibridge, D. Byrne, M. Naeije, and G. Mitchum (2013), Rads: Consistent multi-mission products, in Proc. of the Symposium on, vol. 20, p. 4.

G. Schwarz. Estimating the dimension of a model. Ann. Statist., 6(2):461–464, 03 1978. doi: 10.1214/aos/1176344136.

Sjöberg, L. (2005), A discussion on the approximations made in the practical implementation of the remove–compute–restore technique in regional geoid modelling, Journal of Geodesy, 78(11-12), 645–653.

D. Stephenson, V. Pavan, M. Collins, M. Junge, R. Quadrelli, and Participating CMIP2 Modelling Groups. North Atlantic Oscillation response to transient greenhouse gas forcing and the impact on european winter climate: a CMIP2 multi-model assessment. Climate Dynamics, 27(4):401–420, 2006.

H. v. Storch and F. W. Zwiers.Statistical Analysis in Climate Research. Cambridge University Press, 1999. doi: 10.1017/CBO9780511612336.

G. Taburet, A. Sanchez-Roman, M. Ballarotta, M.-I. Pujol, J.-F. Legeais, F. Fournier, Y. Faugere, and G. Dibarboure. DUACS DT2018: 25 years of reprocessed sea level altimetry products. Ocean Science, 15:12071224, 2019.

Tscherning, C., and R. Forsberg (1986), Geoid determination in the Nordic countries—a status report, in Proc. 10. General Meeting of the Nordic Geodetic Commission, Helsinki, vol. 29, pp. 279–290.

O.Vestøl, J.Ågren, H. Steffen, *et al.* NKG2016LU: a new land uplift model for Fennoscandia and the Baltic Region. *Journal of Geodesy* **93,** 1759–1779 (2019). doi:10.1007/s00190-019-01280-8

D. S. Wilks. Statistical methods in the atmospheric sciences. International geophysics series ; v. 91. Academic Press, Burlington, MA, 2nd ed. edition, 2006. ISBN 0127519661.